

東京大学 大学院新領域創成科学研究科
基盤科学研究系物質系専攻

2021 年度
修士論文

Deposition conditions and Crystallinity of Pyrochlore Iridate
Thin Films

パイロクロアイリジウム酸化物薄膜の堆積条件および結晶性の評価

2021 年 7 月 20 日提出
指導教員 Mikk Lippmaa 教授

余 賢明
Yu Xianming

Abstract

Keyword: Pyrochlore, Iridate, Pulsed laser deposition, Spin-orbit coupling, Topological material

1. Introduction

Strongly-correlated electron systems have been among the most important fields of research in modern condensed matter physics ever since the Mott insulators were discovered. Besides electron correlations, spin-orbit coupling (SOC), which is especially notable in $5d$ systems, is the key to bringing about nontrivial physics, such as topological materials. It has recently been realized that electron correlations, although weaker than in $3d$ systems, still play an important role in $5d$ transition metal oxides, making this class of materials advantageous for studying cooperative effects of electron correlations in the presence of strong SOC. As a high-profile example, pyrochlore iridates of the $R_2\text{Ir}_2\text{O}_7$ family, where R is a rare-earth element such as Y, Eu, Sm, Nd, or Pr, have been intensively studied. Pyrochlores are also famous for the 3-dimensional geometric frustration.

In particular, $\text{Pr}_2\text{Ir}_2\text{O}_7$ is the only member of the iridate pyrochlore series that remains metallic down to mK temperatures because the Pr ion has the largest ionic size among the rare earths that can be used to construct bulk pyrochlores. In this sense, $\text{La}_2\text{Ir}_2\text{O}_7$, due to the even larger ionic radius of La, is expected to be more exotic. Nonetheless, the large ionic radius makes $\text{La}_2\text{Ir}_2\text{O}_7$ unstable in bulk. Therefore, the only possible way to study this material is to synthesize in thin film form.

The electronic structure of $\text{Pr}_2\text{Ir}_2\text{O}_7$ is quite unusual. The bulk crystal shows quadratic band touching close to the Fermi level at the Γ point, which can be detected by the angle-resolved photoemission spectroscopy (ARPES). It is thus a Luttinger semimetal and a parent phase for diverse topological states that may appear by breaking different symmetries. For instance, a topological insulator phase can be induced by applying strain or Weyl nodes may appear if the time-reversal symmetry is broken by applying a magnetic field.

To observe significant electronic structure changes upon structural symmetry reduction, elastic strains on the order of 1% are required. This level of crystal deformation cannot be achieved in bulk crystal without fracturing. Moreover, an ARPES measurement is imperative for detecting the changes in the band structure change caused by lattice deformation. A high-quality stoichiometric crystal surface is therefore required. Thin films can fulfill the strain and stoichiometry requirements, but the only examples of iridate pyrochlore films so far have been synthesized by solid-phase epitaxy, which does not produce a stoichiometric surface and offers limited control over epitaxial strain.

2. Experiments

Iridate thin films were grown by Pulsed Laser Deposition (PLD) using a 248 nm KrF laser. Yttria-stabilized zirconia (YSZ) was selected as the substrate material because the YSZ lattice constant of 10.278 Å is only about 1.1% smaller than that of $\text{Pr}_2\text{Ir}_2\text{O}_7$ (10.394 Å). A commercial praseodymium oxide target and self-made mixed-oxide (Pr or La, Ir)Ox targets were made by Spark Plasma Sintering (SPS) in Kimura laboratory. The effect of the film growth temperature (700°C – 1000°C) and background pressure (0.01 mTorr – 50 mTorr) on the crystal structure was investigated by growing a set of samples and measuring symmetric out-of-plane X-ray diffraction (XRD) patterns with a laboratory Cu K_α x-ray source. The surface morphology of the films was studied by atomic force microscopy (AFM). Furthermore, instead of a pure oxygen gas environment, various oxygen-inert gas mixtures were used to control the kinetic energy of the atoms in the ablation plasma plume.

3. Results and Discussion

By annealing the YSZ substrates in air at 1250°C for 2 hours, a high-quality step-terrace surface was formed as shown in Figure 1.

Figure 2 shows the phase change with the increase of oxygen pressure during film growth at 1000°C. The dashed line in Figure 2 indicates the expected pyrochlore phase position on the left-hand side of the YSZ substrate peak. The peaks at lower angles belong to different praseodymium oxides. Higher substrate temperatures and low oxygen pressures are appropriate for the formation of the pyrochlore phase, but may also result in the generation of a segregated iridium metal phase. Several unknown peaks appear in the XRD result, which are considered to be various nonstoichiometric praseodymium oxides, the relative contributions of which depend on the oxygen pressure, for instance, the PrO_x peak near the 25° position.

For better understanding of these phases, a series of films were grown from a pure Pr_2O_3 target as shown in Fig. 3, which precisely match the several unknown phases and phase change in Figure 2. Moreover, it appears that the valence of praseodymium can easily change with the oxygen pressure, which may be a key factor in the formation of the pyrochlore phase.

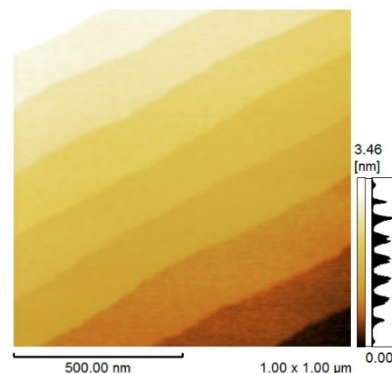


Fig. 1 YSZ substrate after annealing

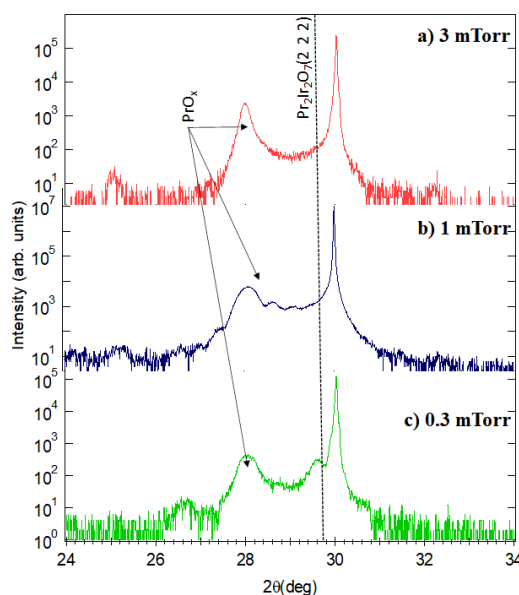


Fig. 2 XRD 2θ-θ scans of $\text{Pr}_2\text{Ir}_2\text{O}_7$ films grown at different PO_2 at 1000°C.

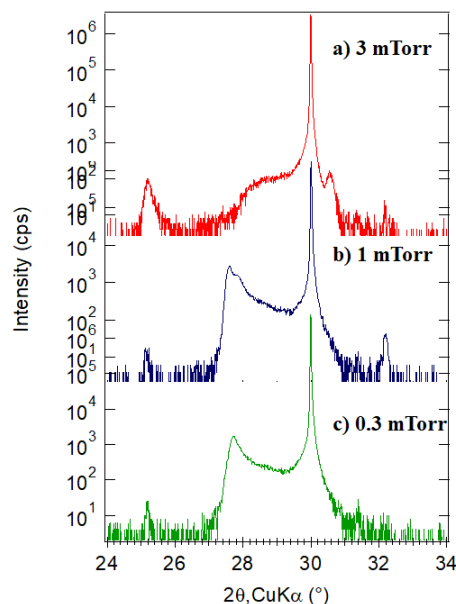


Fig. 3 XRD 2θ-θ scans of Praseodymium Oxides grown at different PO_2 at 1000°C.

There is only a very narrow process window for the pyrochlore phase to form due to the presence of volatile Ir oxides. If the oxygen pressure is too high or too low, either a pure metal phase will segregate or Ir forms IrO_3 , which sublimates rapidly. For eradicating the impact of the iridium metal phase, an inert gas mixture was used to reduce possible resputtering effects of the film surface. The results indicate that inert gas can effectively reduce iridium metal segregation.

Compared with Pr, the valence of La is relatively stable +3 in most cases. Therefore, it may be easier to fabricate a $\text{La}_2\text{Ir}_2\text{O}_7$ thin film. The experiment results have verified the stability of La's valence; however, further research is required to understand Ir clustering during $\text{La}_2\text{Ir}_2\text{O}_7$ growth.

Metal segregation during film growth is a kinetic process, influenced by the ablation pulse rate. Even when the laser pulse rate was 10 Hz, an iridium metal peak with high intensity still appeared in XRD, which indicates that the clustering speed of iridium is much higher than the usual estimates for oxide surface diffusion and leads to phase separation. On the other hand, the Ir metal peak intensity drops gradually with the decrease of frequency as shown in Fig. 4. This is strong evidence that evaporation of iridium happens on the film surface if the growth rate is very low. This behavior matches the results of a recent calculation, which showed that the [111] facet of iridium has the highest oxidation

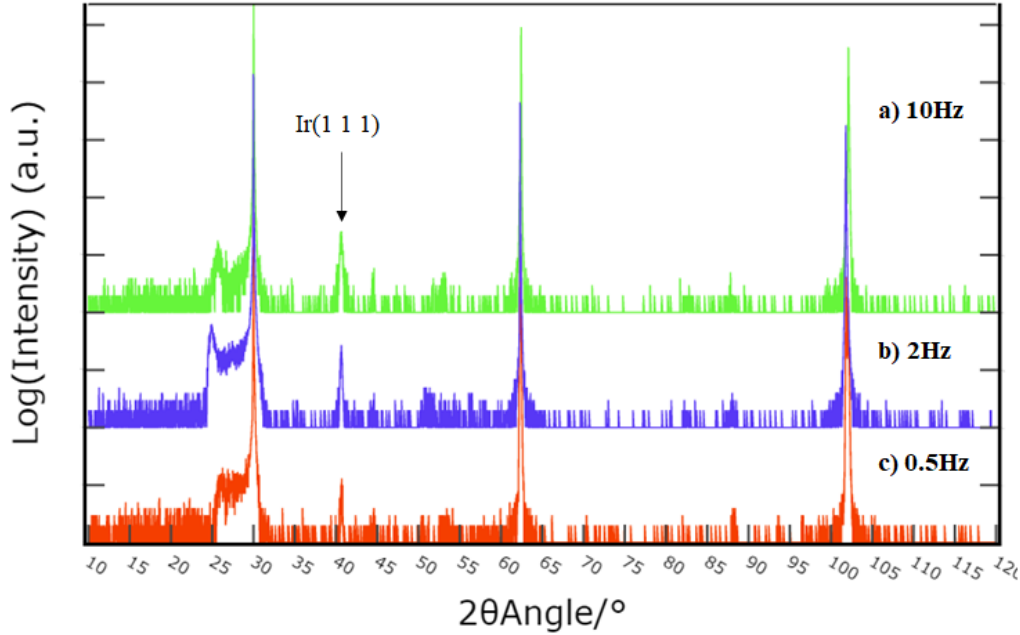


Fig. 4 XRD 2θ scans of the Ir metal peak with different intensity in different laser frequencies. Temperature = 900°C, oxygen pressure = 10mTorr.

rate. Moreover, experiments with interval pulsed laser deposition reveal that a certain number of pulses is required to ensure the stability of iridium clusters even at very high deposition rates. An unstable iridium metal phase is expected to be reactive to rare-earth elements.

4. Conclusion

In this work, the control of the A-site ion valence was found to be crucial for the formation of the pyrochlore phase, which is extremely sensitive to the oxygen partial pressure in the case of Pr. Additionally, in contrast to the naïve conjecture that the difficulty of growing pyrochlore iridate is caused by the volatility of iridium, the research of iridium behavior indicates that clustering is the biggest obstacle in this experiment, which is also possible for other 2-dimensional iridate materials when grown along the [1 1 1] direction. Moreover, it appears to be possible for unstable iridium cluster to form at certain growth conditions, which may be the key to achieving direct PLD growth of stoichiometric pyrochlore iridate films.

References

- [1] R. Schaffer *et al.*, Rep. Prog. Phys. **79**, 094504 (2016).
- [2] T. Kondo *et al.*, Nature Commun., **6**, 10042 (2015).
- [3] X. Hou *et al.*, Journal of Crystal Growth, **46**, 24–2825 (2017).
- [4] I. Seo *et al.*, Computational Materials Science, **184**, 109897 (2020)

Contents

Abstract	1
Chapter 1. Introduction.....	5
1.1. Strongly-correlated systems and Spin-orbit coupling	5
1.1.1. Strongly-correlated systems and the Hubbard model	5
1.1.2. Spin-orbit coupling	7
1.1.3. Novel quantum materials with SOC	9
1.1.4. Angle resolved photoemission spectroscopy	13
1.2. Pyrochlore Iridates	15
1.2.1. The pyrochlore structure	15
1.2.2. Pyrochlore iridates	18
1.3. Propose of the thesis	21
Chapter 2. Methods.....	23
2.1. Thin film growth	23
2.1.1. Pulsed laser deposition.....	23
2.1.2. Solid-phase Epitaxy	27
2.2. Target synthesis	28
2.3. Characterization.....	31
2.3.1. Atomic force microscope	31
2.3.2. X-ray diffraction	32
Chapter 3. Growth of $R_2Ir_2O_7$ ($R = Pr, La$).....	35
3.1. Substrate	35
3.2. Growth of $Pr_2Ir_2O_7$	36
3.2.1. Deposition with a solid-state reaction target.....	36
3.2.2. Depositions with spark plasma sintering target	41
3.2.3. Depositions with a Pr_6O_{11} target	44
3.2.4. Depositions in an inert gas	46
3.3 Growth of $La_2Ir_2O_7$	53
Chapter 4. Influence of iridium clustering	56
Chapter 5. Summary	60
Acknowledgements.....	61
References.....	62

Chapter 1. Introduction

1.1. Strongly-correlated systems and Spin-orbit coupling

1.1.1. Strongly-correlated systems and the Hubbard model

Although the behavior of many metallic materials can be adequately described by the conventional energy band picture¹ (Figure 1.1a), a class of transition metal oxides was discovered in the 1930s that exhibited insulating behavior despite having a partially filled energy band². To solve this issue, Mott propound a model that considers the effects of electron-electron correlations that lead to the opening of an energy gap due to the Coulomb interaction among the valence electrons³(Figure 1.1b). This kind of insulator is thus known as a Mott insulator but there is still no perfect theory to fully understand the physics behind the behavior of Mott insulators. More broadly known as strongly-correlated systems, materials where conduction electron correlations play an important role in defining the materials characteristics still attracted extensive interests in condensed matter physics. A well-known example is the group of cuprate high- T_c superconductors⁴.

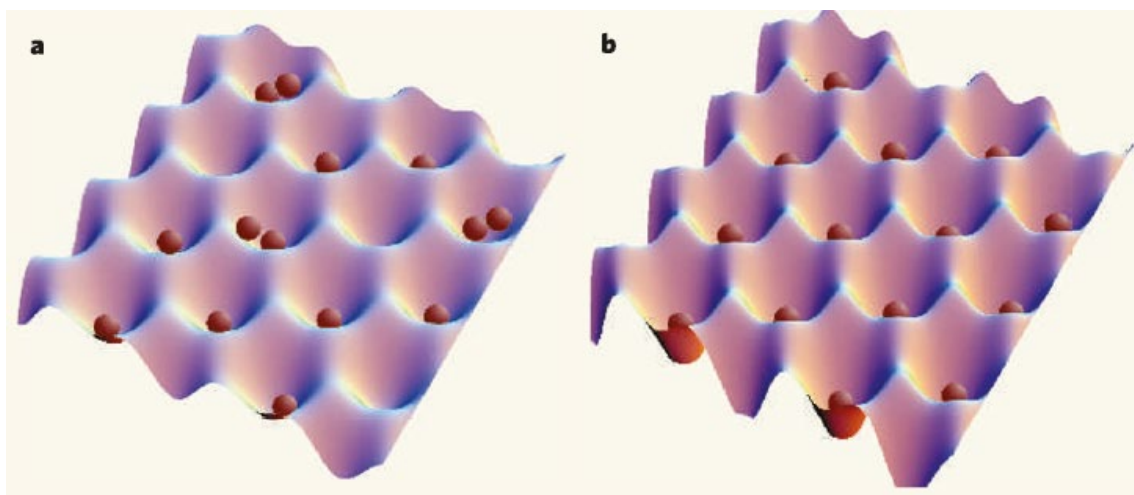


Figure 1.1(a) Regular potential wells of normal metallic phase (b) the Mott insulator phase¹

The Hubbard model is a simple lattice fermion model that can effectively describe the Mott phase transition as well as interactions among electrons⁵. The model includes only two terms: an electron hopping terms to denote the kinetic energy and a repulsion term to describe the interaction. Its Hamiltonian in a second-quantized form is given by

$$\begin{aligned}\mathcal{H}_H &= \mathcal{H}_t + \mathcal{H}_U - \mu N \\ \mathcal{H}_t &= -t \sum_{\langle ij \rangle} (c_{i\sigma}^\dagger c_{j\sigma} + \text{H.c.}) \\ \mathcal{H}_U &= U \sum_i \left(n_{i\uparrow} - \frac{1}{2} \right) \left(n_{i\downarrow} - \frac{1}{2} \right) \\ N &\equiv \sum_{i\sigma} n_{i\sigma},\end{aligned}$$

where the last term is the chemical potential that determines the position of the Fermi level and the parameter t is the integral describing the probability of electrons hopping, which is proportional to the band width. U denotes the Hubbard interaction, the increase of which corresponds to an increase of the repulsion between electrons within the same lattice point.

If the hopping term is not sufficient to counteract the interaction term, electrons will be forced to occupy different lattice points. In the case of a half-filled band, every point is occupied on average by a single electron, which can further result in a band splitting, as shown in Figure 1.2a. The gap between the two split bands is called the Mott gap and the material enters a Mott insulator phase.

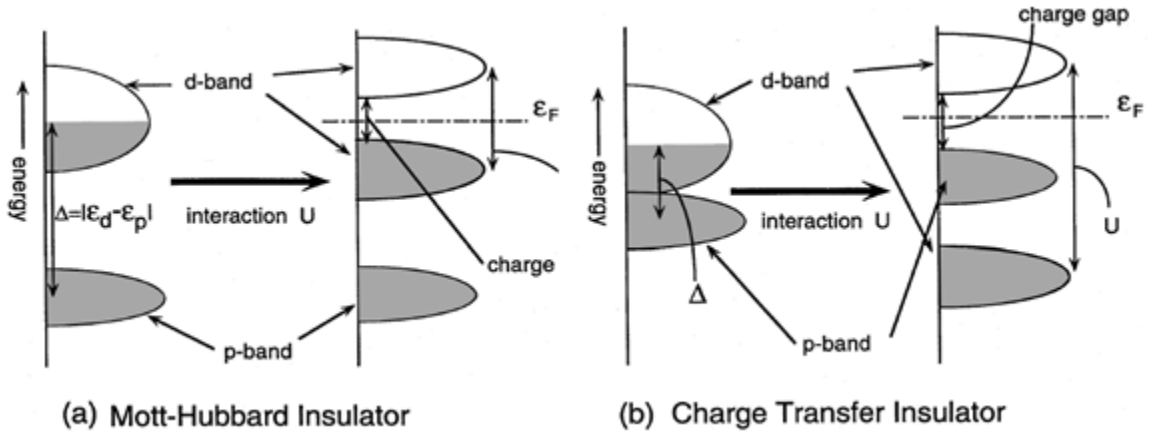


Figure 1.2 Schematic illustration of energy levels for (a) Mott-Hubbard Insulator and (b) Charge Transfer Insulator².

A different type of Coulomb repulsion can be found in another type of insulator, known as a charge transfer insulator. The mechanism is similar to a Mott insulator but with a different band configuration. Since the repulsion is bigger than the transfer energy between the d -orbital and oxygen's p -orbital, electron hopping tends to occur between metal ions and oxygen ions. Consequently, the lower Hubbard d -band should be below the oxygen $2p$ band in energy as shown in Figure 1.2b.

Research based on the Hubbard model has led to huge progress in the understanding of the behavior of many transition metal oxides besides the cuprates mentioned earlier. Numerous quantum phenomena can be explained by this model, including metal-insulator transitions (MIT), long range magnetic order, superconducting phase transition, and the quantum critical effect. The versatility of the Hubbard model is partly due to the interaction between holes in the metal d band and the neighboring oxygen p bands, which leads to what is known as Zhang-Rice singlet.⁶ For several transition metal oxides, the electronic description can therefore adequately approximated with a single-band Hubbard model⁷.

1.1.2. Spin-orbit coupling

Conventionally, it is understood that $4d$ and $5d$ electrons have a much weaker Hubbard interaction in the spatially extended d orbitals. Nonetheless, anomalous insulator behavior can also be found in $5d$ transition metal oxides⁸. Spin-orbit coupling (SOC), a relativistic effect, is considered to play an important role in these $5d$ electron systems while it can be mostly neglected in the description of the lighter $3d$ materials. As mentioned above, the Hubbard interaction is proportional to the band width, hence it is reasonable to have a narrow band width near the Fermi surface considering the energy level splitting in the presence of a strong octahedral crystal field, as shown in Figure 1.3⁹.

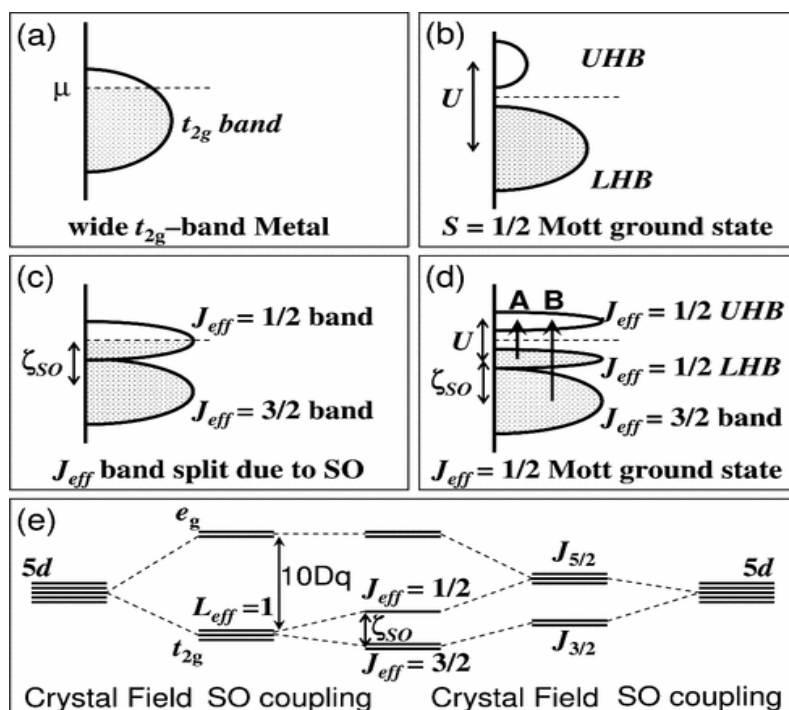


Figure 1.3 Schematic energy diagrams for the $5d^5 (t_{2g})$ electronic configuration (a) without SO and U , (b) with an unrealistically large U but no SO, (c) with SO but no U , and (d) with SO and U . (e) $5d$ level splittings by the crystal field and SO coupling.

SOC describes the interaction between spin angular momentum and the orbital angular momentum. The movement of an electron inside an atom can generate an apparent magnetic field that will interact with the intrinsic spin magnetic moment of the electron. The Hamiltonian can be simply given by¹⁰

$$\mathcal{H}_{\text{so}} = \lambda \mathbf{S} \cdot \mathbf{L},$$

where \mathbf{S} denotes the spin angular momentum, \mathbf{L} denotes the orbital angular momentum, and λ is the spin-orbit coupling constant that is proportional to Z^4 , where Z is the atomic number. In general, the spin-orbit coupling strength for $5d$ electrons can be 100 times higher than for $3d$ electrons, as shown in Figure 1.4¹¹.

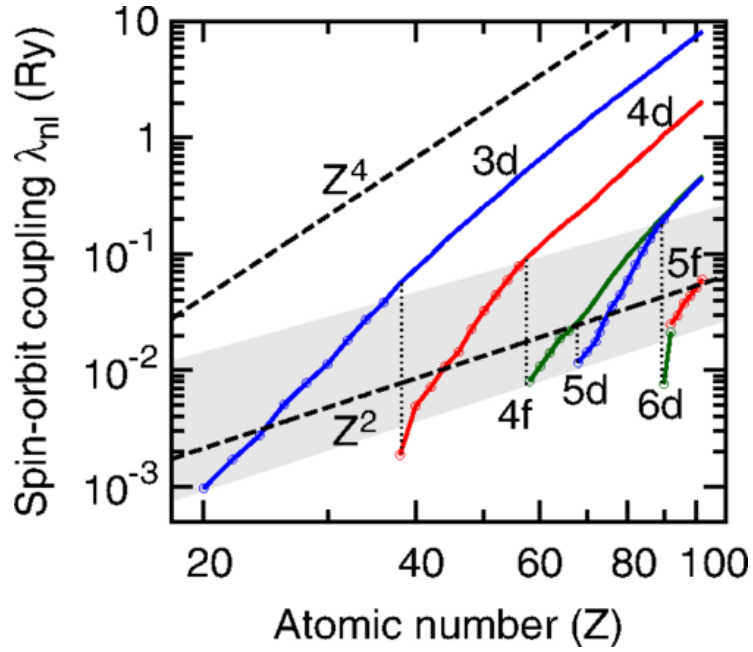


Figure 1.4 Dependence of the spin-orbit coupling strength λ on the atomic number Z .

1.1.3. Novel quantum materials with SOC

Due to the consideration of spin, SOC can break the spin-SU(2) symmetry, which brings a variety of new physics¹². Figure 1.5¹³ shows the rich phases of spin-orbit coupled Mott insulator. In this thesis, only some of them will be discussed.

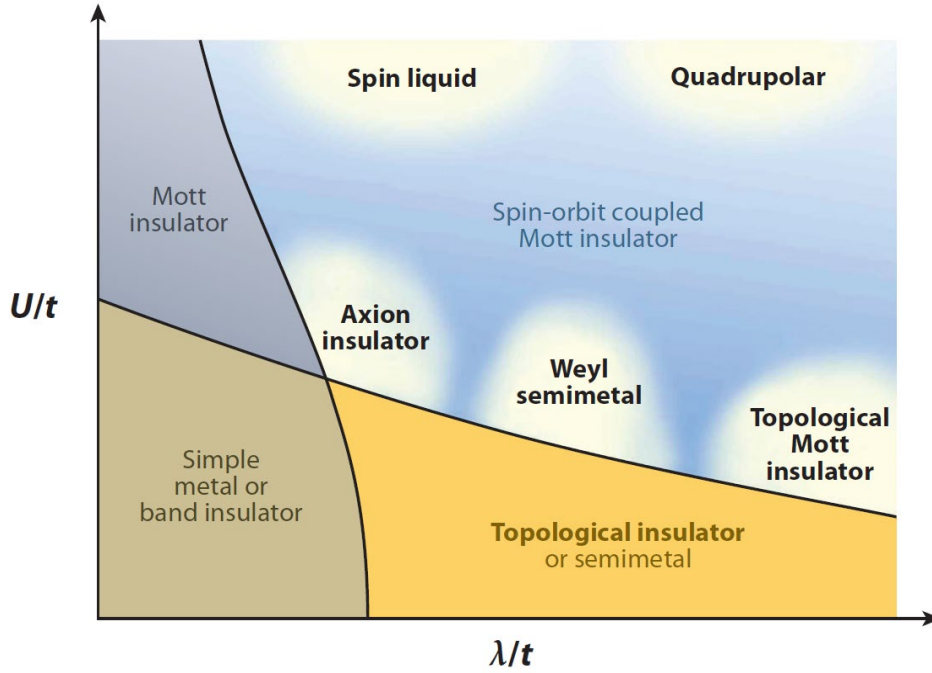


Figure 1.5 Phase diagram of electronic systems considering both correlation strength and SOC.

1.1.3.1. Topological insulator

The Quantum Hall effect, which was observed in 1980, unveiled a new conductive edge state¹⁴ that suggested that there may be new materials beyond simple metals and insulators. A simple image of the edge states is shown in Figure 1.6a¹⁵. Under a strong magnetic field, electrons will move on a circular path with a field-dependent radius due to the Lorentz force. Inside a material, absent scattering, an electron would be forced to go around in circles, while electrons near a surface would collide with the discontinuity at the edge of a crystal and then continue to move on a semicircular path. In this model, long-range currents can only be sustained near the edges while the bulk would remain insulating. The states supporting the flow of current are known as edge states. The movement of electrons only occurs along one direction, which is not be affected by scattering from impurities or defects, so there is almost no

dissipation or generation of heat. The QHE has pointed out a promising way for developing new electronic device in the future.

In practice, observing the QHE requires an extremely low temperature and a strong enough magnetic field. In 2005, Kane and Mele's theoretical computation predicted that an energy gap would be generated by the SO interaction near the Dirac point of monolayer graphene¹⁶, which should leads to a Quantum Spin-Hall (QSH) Effect. The QSH effect allows a material to possess a conducting edge state, which is related to the spin direction and is preserved by the time-reversal symmetry. As shown in Figure 1.6b, electrons with opposite spin directions would travel in opposite directions.

The edge states can be described by topological concepts of geometry which originally focus on the preserved geometric properties during a continuous shape deformation. A typical example is a donut, which is topologically homotopic with a coffee cup but is not homotopic with a ball in the sense that the hole in the donut or the coffee cup is a topological invariant. For electronic materials, the band structure of QSH graphene is not homotopic with a normal insulator. Thus, the bands associated with edge states are described as being topologically non-trivial bands and the materials that possess such edge states are known as topological insulators.

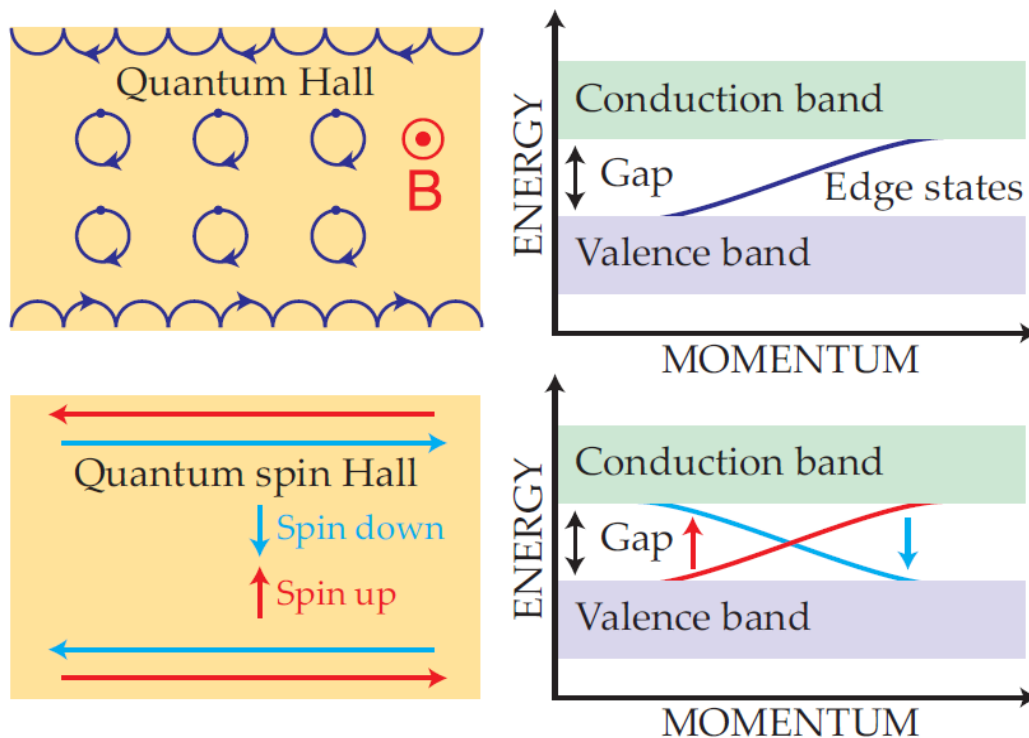


Figure 1.6 (a) Schematic of Quantum Hall effect (b) Schematic of Quantum spin Hall effect

1.1.3.2. Topological semimetal

The understanding of the topological insulator state naturally led to the concept of a semimetal. The requirement for a topological semimetal state is a band near the Fermi level that satisfies the linear dispersion relation of the Dirac or Weyl equation. The characteristic feature of such an electronic system is the existence of band touching points between the conduction and valence bands in the momentum space, which are known as Dirac or Weyl points¹⁷. A Dirac point is preserved in the presence of both time-reversal symmetry and inversion symmetry but can evolve into a pair of non-degenerate chiral Weyl points if either symmetry is broken. Figure 1.7 shows a pair of Weyl points (right) generated from a Dirac point (left) by breaking the p-symmetry¹⁸.

Because the band is preserved by topology and has a linear dispersion relation, the Weyl semimetal can present various peculiar phenomena. One important characteristic is the discontinuous topological Fermi arc associated with the edge states, which forms a connection between a pair of chiral Weyl points (Figure 1.7 right). A Weyl point is the source or a drain of the Berry curvature and can be considered as an equivalent of a magnetic monopole in the momentum space, which has been argued to result in unusual magnetoelectric coupling that affect the transportation properties including the anomalous Hall effect (AHE)¹⁹, negative magnetoresistance induced by a chiral anomaly²⁰, and surface related quantum oscillations.²¹

A Weyl semimetal can be classified into two types according to breaking of different symmetries. The first experimental realization is the non-magnetic Weyl semimetal TaAs, which is generated by breaking the inversion symmetry.^{22,23} The earliest theoretical prediction is the appearance of a magnetic Weyl semimetal state in pyrochlore iridates.²⁴ However, this

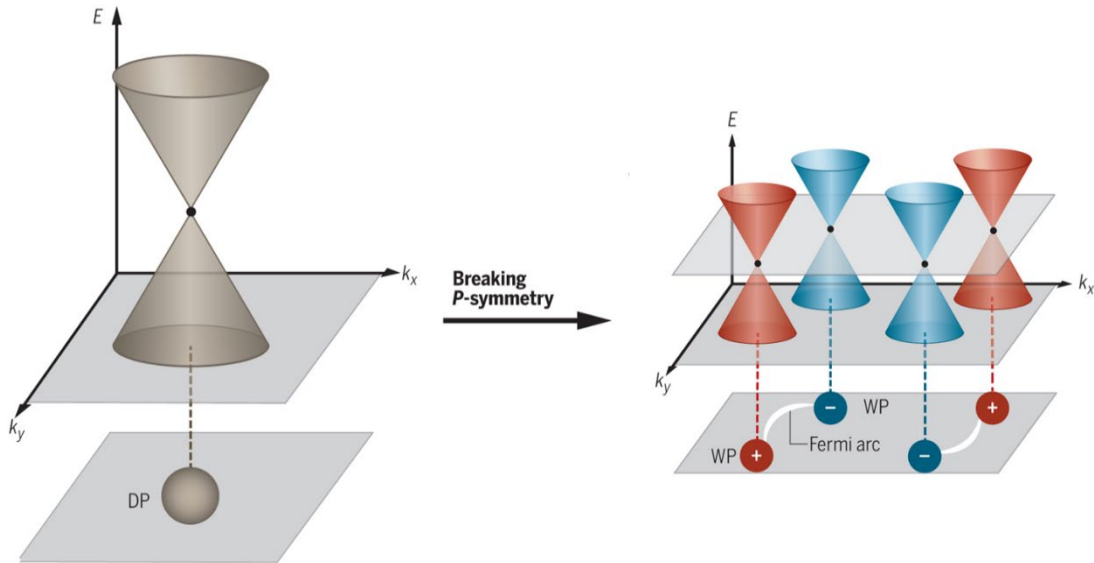


Figure 1.7 Weyl points and fermi arcs (left) generated from Dirac point (right) by breaking the p-symmetry

state was found only quite recently²⁵. A magnetic Weyl semimetal is closely related to the Chern insulator state which can be utilized in the quantum anomalous Hall effect (QAHE)²⁶. Moreover, it allows the minimum number of Weyl points (only one pair of Weyl points), which might be favorable for experimental research on Weyl fermions.

1.1.3.3. Quantum spin liquid

In 1973, P. W. Anderson developed the concept of a quantum spin liquid (QSL) to describe the behavior and properties of a triangular antiferromagnetic lattice.²⁷ The assumption in a triangular Heisenberg model is that if spins at two vertices of a triangle are fixed to opposite directions, there will be a frustration associated with the spin at the third vertex spin as shown in Figure 1.8. Anderson pointed out that one possibility is a disordered ground state which consists of several degenerate spin states. This so-called resonating valence bond model has the minimum energy and is the prototype of a spin liquid. Although this model was proven to have a minimum energy in a Néel order,²⁸ spin liquids have become a new field of study in condensed matter physics.

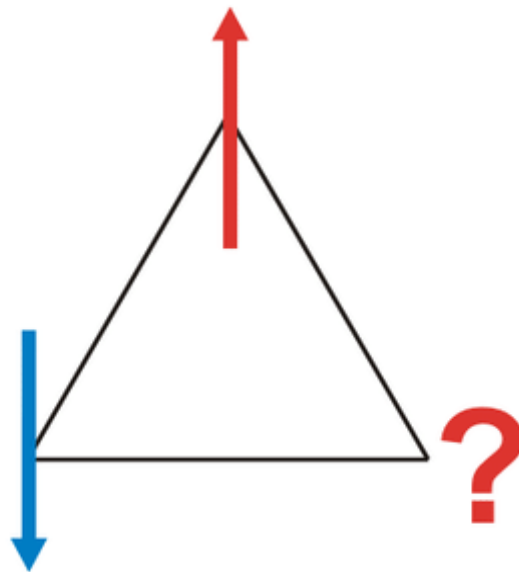


Figure 1.8 Spin frustration in a triangular lattice

For regular magnetic materials, with the decrease of temperature, the thermal fluctuations decrease until the material forms an ordered low-energy state due to the interaction among magnetic moments. The temperature at which this happens is known as the Curie temperature or the Néel temperature. For a QSL, geometrical frustration will prevent it from forming an ordered state even at absolute zero. In this system, spins are continuously fluctuating without

a certain direction, similar to molecules in a liquid. One of the interesting points of a QSL is that this phase transition cannot be describes by Landau's phase transition theory, which assumes that a phase transition is always accompanied by symmetry change, while there is no symmetry change in transition between a paramagnetic spin state and a low-temperature QSL.

Most QSL models are based on the Heisenberg model, ignoring the strongly anisotropic interaction arising from SOC.²⁹ YbMgGaO₄ is an example of a quantum spin liquid in a triangular lattice Heisenberg model and is observed to have an antiferromagnetic exchange interaction at 4 K but does not show any ordered state even down to 60mK.³¹ Experiments have revealed that an effective 1/2 spin Hamiltonian³² describes the system as well as the spinon excitations by neutron scattering³³. Figure 1.9 shows the crystal structure of YbMgGaO₄.

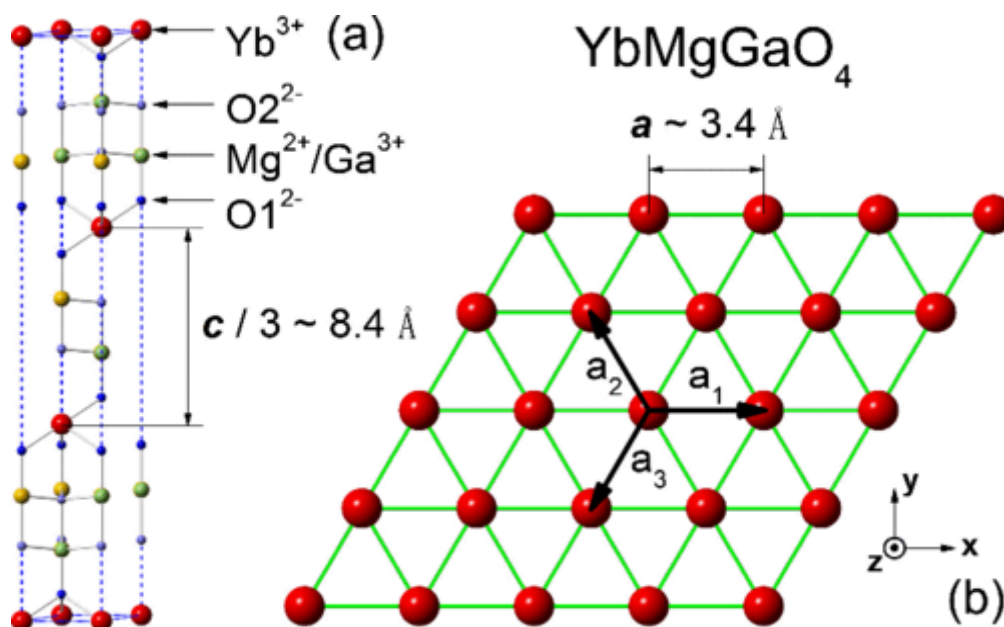


Figure 1.9 The lattice structure (a) and ab plane (b) formed by Yb ions of YbMgGaO₄

1.1.4. Angle resolved photoemission spectroscopy.

One effective experimental technique for the study of topological materials is angle-resolved photoemission spectroscopy (ARPES). ARPES utilizes the photoelectric effect. When the photon energy of light incident on a surface is higher than a certain value, free photoelectrons can be ejected from the surface into vacuum. The critical photon energy value is called the work function of a material. The emitted photoelectrons can be collected and measured to obtain an angle-dependent energy distribution that reflects the energy distribution of electrons in the solid. Figure 1.10 shows the mechanism of ARPES³⁴. From the law of conservation of energy, a formula can be written as $\hbar\omega = E_{\text{kin}} + \phi + E_{\text{B}}$, where the $\hbar\omega$ is the energy of

incident light, E_{kin} is the kinetic energy of a photoelectron, ϕ is the work function and E_B denotes the electron's binding energy. Except for E_B , other terms can be observed and measured, from which E_B can be calculated. When an electron is emitted from the surface, the momentum component parallel to the sample surface is preserved and the photon's momentum can be neglected, which can be written as

$$\mathbf{p}_{\parallel} = \hbar \mathbf{k}_{\parallel} = \sqrt{2m_e E_{\text{kin}}} \cdot \sin \theta,$$

where \mathbf{p}_{\parallel} is the component of the electron momentum parallel to the direction of the crystal lattice, \mathbf{k}_{\parallel} is the wave vector component in this direction, m_e is the mass of the electron and θ is the angle between the incident direction and the surface normal. By analyzing the energy and momentum of photoelectrons, the dispersion relation can be calculated as well as the Fermi surface of the sample.

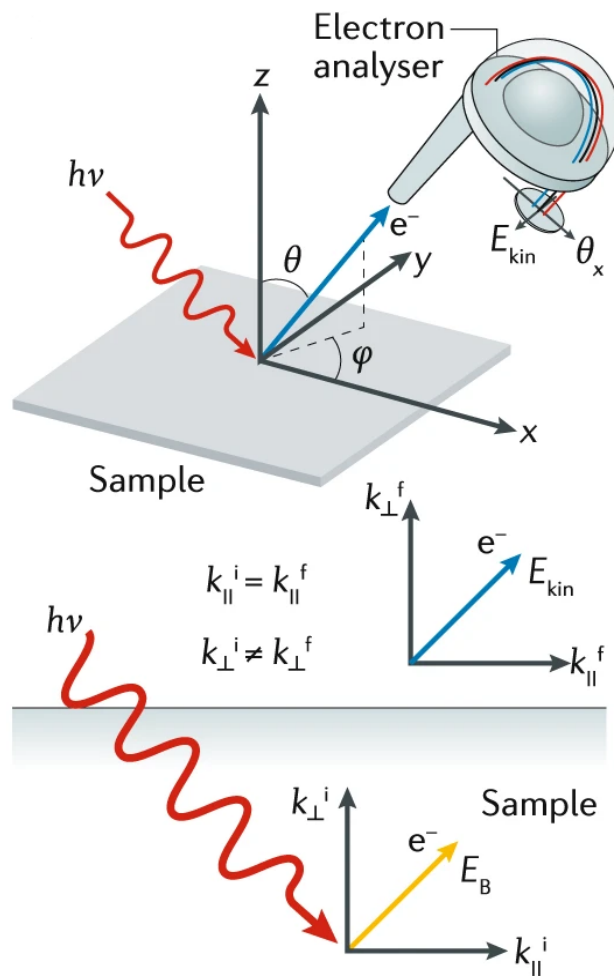


Figure 1.10 Mechanism of ARPES

ARPES is the most direct measurement for detecting the dispersion relations of surface states which shows characteristics of topological materials, such as the presence of Dirac points or Dirac cones near the Fermi surface. However, ARPES is a very surface sensitive technique that can only observe electrons emitted from a thin surface layer. The surfaces also have to be atomically flat, at least on certain length scales. These requirements limit the types of materials that can be analyzed by ARPES.

1.2. Pyrochlore Iridates

The pyrochlore structure makes a particularly advantageous platform for studying the effects of geometric frustration — the special lattice of corner-sharing tetrahedra can form a kagome lattice in the $[111]$ direction. For this thesis work, another important feature is that a strong SOC can be introduced to the structure by using $5d$ transition metal ions such as Ir^{4+} , which opens the possibility of studying a variety of novel quantum phenomena³⁵.

1.2.1. The pyrochlore structure

The general chemical formula of pyrochlore oxides is $\text{A}_2\text{B}_2\text{O}_7$, where the A-site cation is a rare earth ion and the B site is occupied by a transition metal ion. There are two types of pyrochlore³⁶, $\text{R}_2^{2+}\text{B}_2^{5+}\text{O}_7^{2-}$ and $\text{R}_2^{3+}\text{B}_2^{4+}\text{O}_7^{2-}$, but only the latter will be focused on in this thesis. Pyrochlores have the face-centered cubic (fcc) Bravais lattice, and its space group is $\text{Fd-}3\text{m}$ (No. 227). Figure 1.11 shows the pyrochlore structure using $\text{Nd}_2\text{Ir}_2\text{O}_7$ as an example³⁷, where the red and green colors denote different sublattices formed by the Nd and Ir ions, respectively.

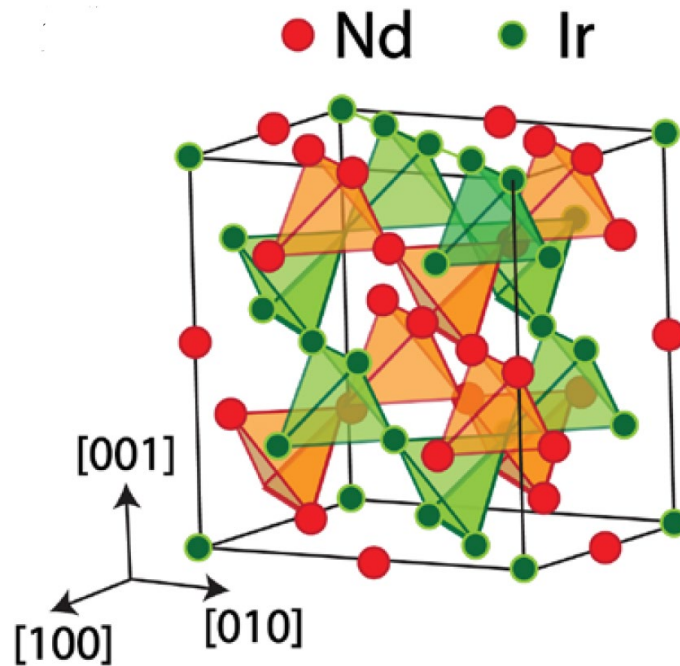


Figure 1.11 Lattice structure of $\text{Nd}_2\text{Ir}_2\text{O}_7$

For oxygen atoms, since there are two inequivalent position, the chemical position can be also written as $A_2B_2O_6O'$. The O corresponds to the Wyckoff 48f ($x, 1/8, 1/8$) position while O' corresponds to 8b ($3/8, 3/8, 3/8$)³⁶. The rare earth ion in the A site forms an A_2O' tetrahedral structure and the transition metal ion at the B site forms an octahedra lattice of B_2O_6 . x is the positional parameter of O that can be slightly changed mainly depending on the radius of the A-site ion. A perfect octahedron can form when x equals 0.3125, which will be compressed along (1 1 1) direction with the increase of x . The typical x value range for pyrochlore iridates is [0.32, 0.345]³⁸. The stability of pyrochlores hinges on the radius of both A- and B-site ions as well as their ratio. Figure 1.12 shows the possible stable pyrochlore phases for different A and B site elements³⁶.

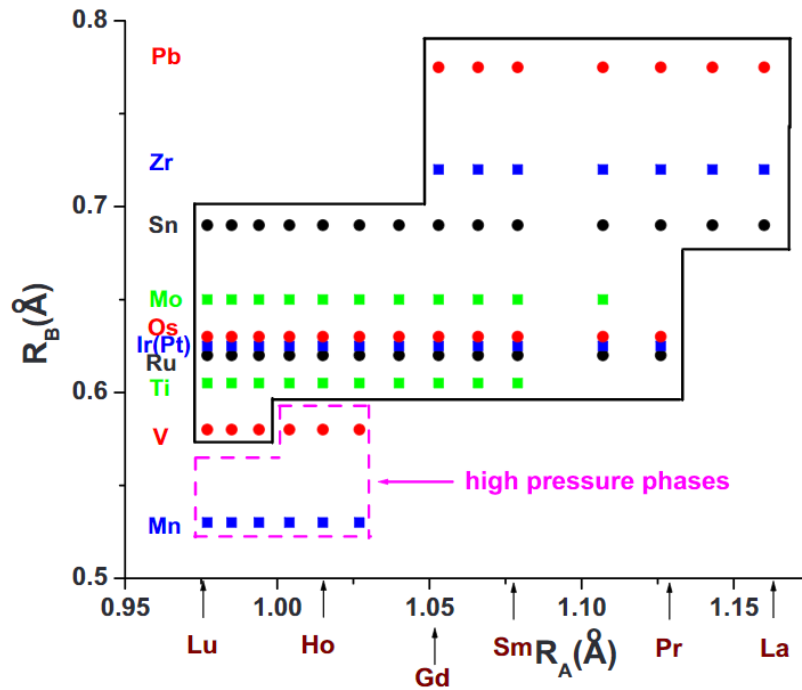


Figure 1.12 A structural stability-field map for $A_2B_2O_7$ materials

Pyrochlores are among the most intensively studied structures for exploring three-dimensional geometrical frustration effects. The structure of corner-sharing tetrahedra brings about more complicated spin configurations and geometrical frustration regardless of the ferromagnetism or antiferromagnetism between neighboring spins, as shown in Figure 1.13³⁹.

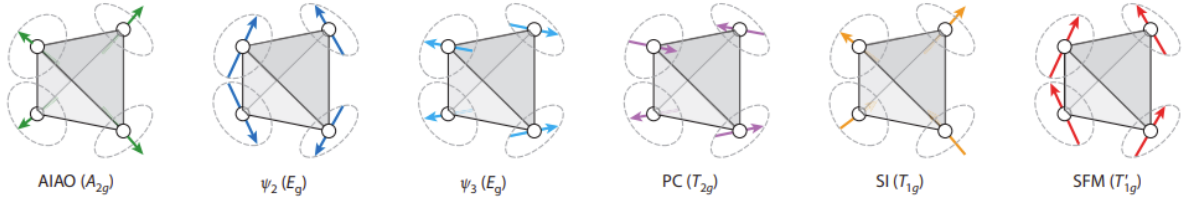


Figure 1.13 Possible spin configuration in pyrochlore. Abbreviations: AIAO, all-in/all-out; PC, Palmer–Chalker; SFM, splayed ferromagnet; SI, spin ice.

Considering the Ising spin model, which is the simplest model for studying geometric frustration, in a ferromagnetic interaction, spins on the vertices of tetrahedra are limited to point along the axis that connects the center and a vertex, stabilizing a 2-in-2-out spin configuration. This configuration is called a spin ice in that it is similar to the relation between hydrogen and oxygen in water ice, as shown in Figure 1.14⁴⁰. In the case of antiferromagnetism, the strong spin fluctuations lead to a spin liquid ground state at low temperature.

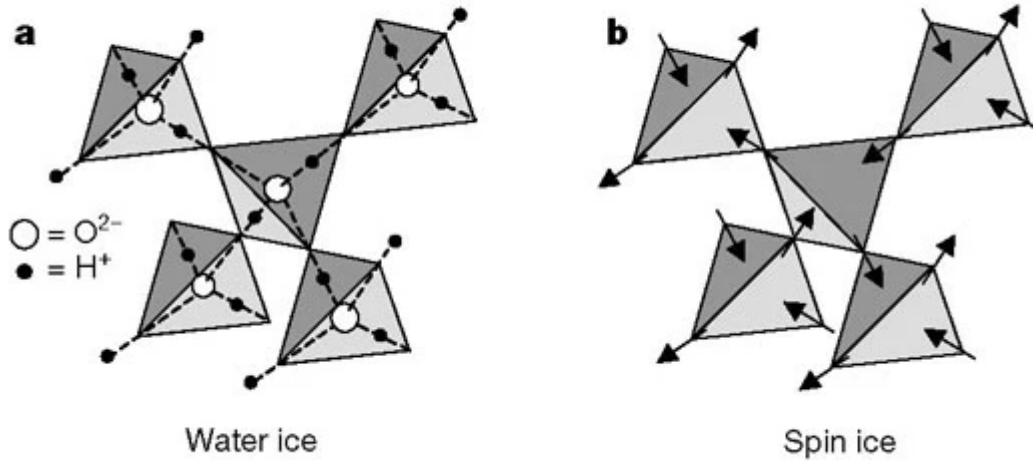


Figure 1.14 Schematic representation of frustration in water ice and spin ice.

An interesting problem in spin ice phases is the question of the types of elementary excitations that can exist. Quasiparticles can be generated if the 2-in-2-out configuration is broken to form a 3-in-1-out or 3-out-1-in configuration, which can be regarded as magnetic

monopole. Different from Dirac's magnetic monopole, the excitons arise from a net magnetic charge inside the tetrahedra and always appear in pairs with opposite signs. Positive and negative monopoles can move in the lattice independently, which are connected by a so-called Dirac string⁴¹.

Apart from the Ising model, there are two other models that may be used to describe spin structures in pyrochlores depending on different A-site rare earth ions⁴². One is the XY model, where spin orientations are vertical along the $[1\ 1\ 1]$ direction. The other is the Heisenberg model, which doesn't limit the spin orientations.

1.2.2. Pyrochlore iridates

The electron configuration of Ir^{4+} is $[\text{Xe}]5d^5$ with $J_{\text{eff}} = 1/2$, $L_{\text{eff}} = 1$ and $S = 1/2$, which makes the pyrochlore iridates an ideal platform for the study of quantum phenomena. There are rich phases for pyrochlore iridates considering the SOC as shown in Figure 1.15²⁴. With the increase of correlation strength, electronic behavior changes from metal to Mott semimetal under low external magnetic fields. Under high magnetic fields, pyrochlore iridates will enter a ferromagnetic metal phase.

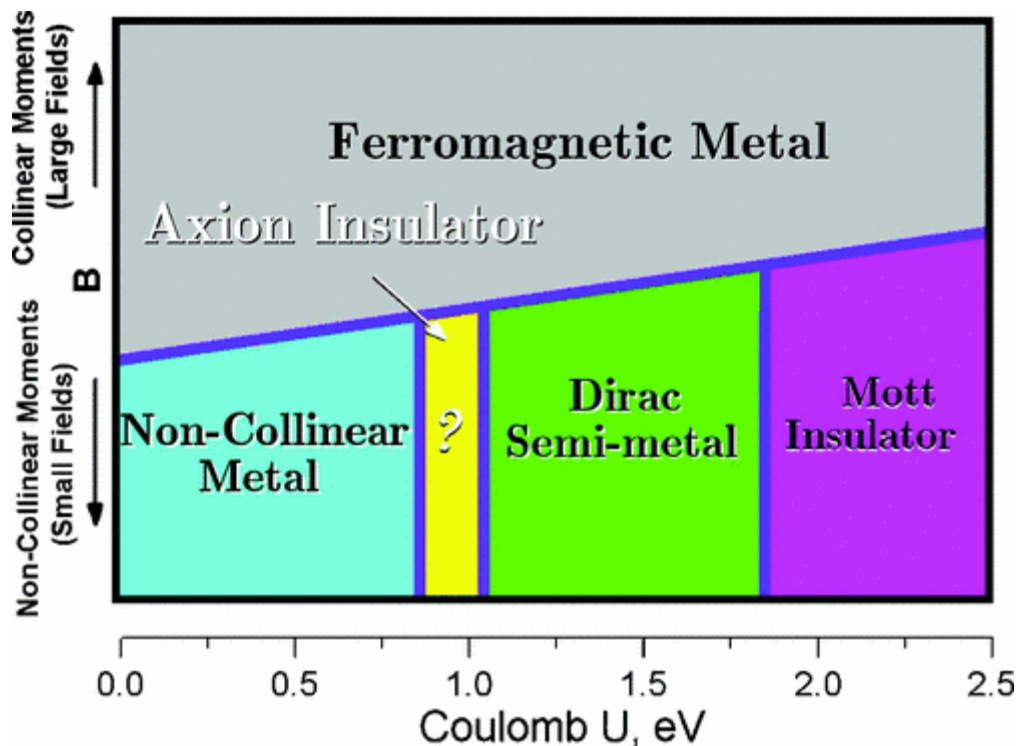


Figure 1.15 Sketch of the predicted phase diagram for pyrochlore iridates.

Research about the metal-insulator transition (MIT) in pyrochlore iridates shows that the MIT temperature is strongly related to the A-site ion^{43,44}, as shown in Figure 1.16 and this MIT

is always accompanied by a magnetic anomaly without changing the structure. Theoretical calculation results indicate that the $4f$ electrons of the A-site rare-earth ion have little influence on the electronic structure, while the length and angle of the Ir-O-Ir bond are changed by the A-site ionic radius, which eventually leads to the change of the crystal structure and a MIT transition²⁴.

Among this family, $\text{Pr}_2\text{Ir}_2\text{O}_7$ is a peculiar one since it doesn't show MIT even at temperatures down to the mK range and metallic spin-liquid behavior as well as Kondo effect are observed in this crystal⁴⁵. Moreover, the breaking of time-reversal symmetry from the 2-in-2-out chiral spin configuration results in a spontaneous Hall effect without measurable magnetization, as shown in Figure 1.17.⁴⁶

ARPES experiment result of bulk $\text{Pr}_2\text{Ir}_2\text{O}_7$ shows a Fermi node formed by quadratic band touching at the Γ point at the Fermi level between the doubly-degenerate valence and conduction bands, forming what is known as a Luttinger semimetal state⁴⁷. The Luttinger semimetal is a well-known parent phase of various topological phases including topological insulators and Weyl semimetals⁴⁸. The electronic structure with a quadratic band touching is sensitive to perturbation such as lattice strain and external magnetic field, which breaks certain symmetries and leads to a phase transition.

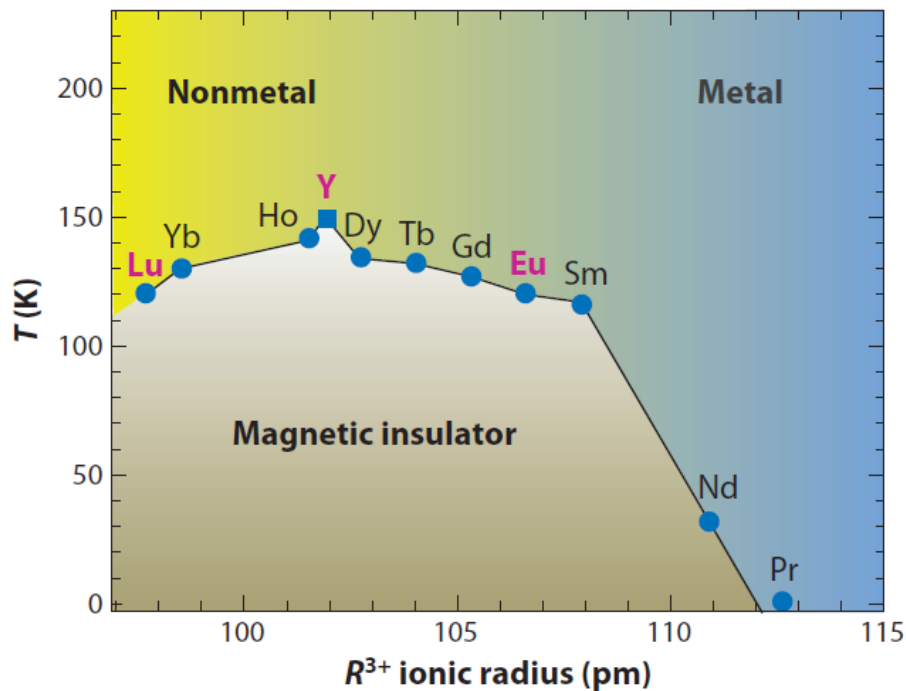


Figure 1.16 Metal-insulator transition temperature of pyrochlore iridates

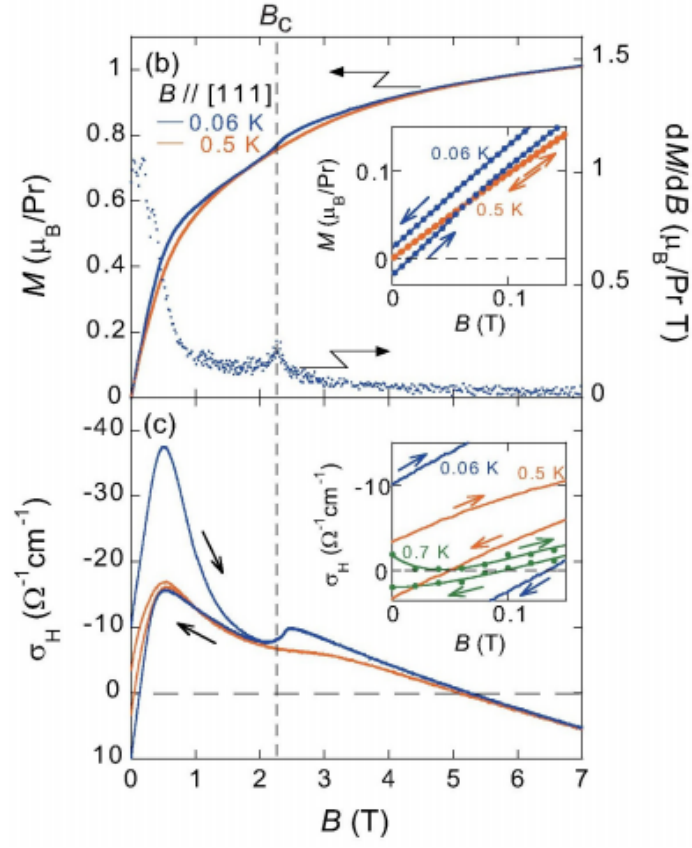


Figure 1.17 Spontaneous Hall effect in $\text{Pr}_2\text{Ir}_2\text{O}_7$

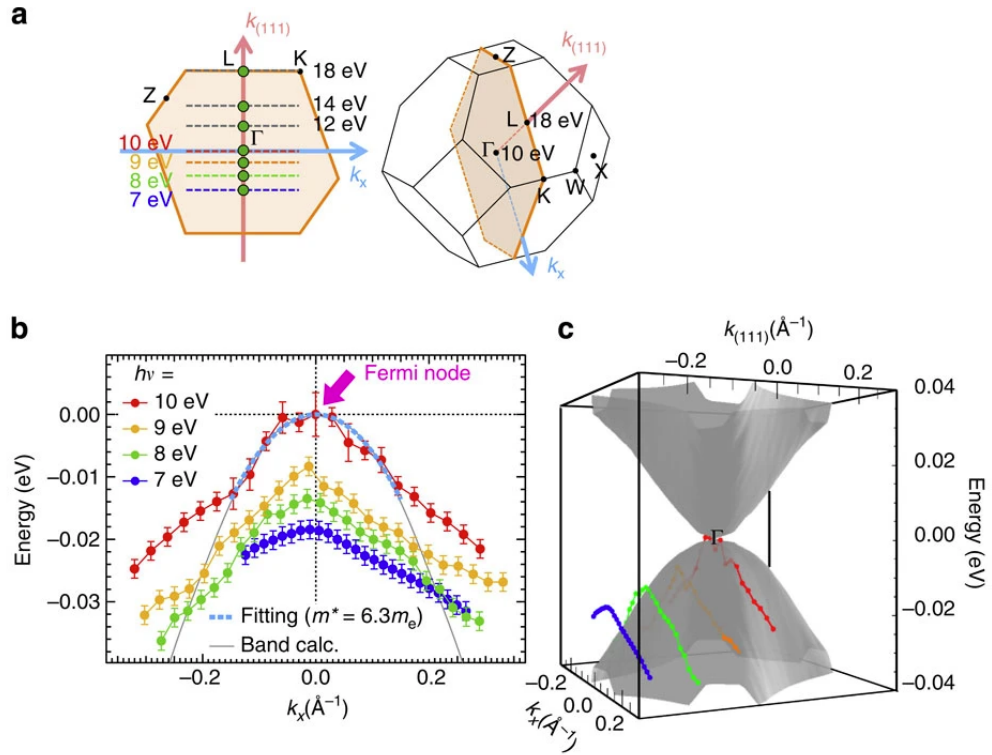


Figure 1.18(a) Brillouin zone of $\text{Pr}_2\text{Ir}_2\text{O}_7$ (b-c) quadratic band touching from ARPES experiments.

In particular, a trigonal lattice distortion can be induced by applying strain, which leads to a topological insulator phase as predicted by theoretical calculation, as shown in Figure 1.19⁴⁹. Moreover, a magnetic Weyl semimetal phase requires a pair of non-degenerate Weyl point which can be induced by breaking the t-symmetry and p-symmetry simultaneously as shown in Figure 1.20⁵⁰.

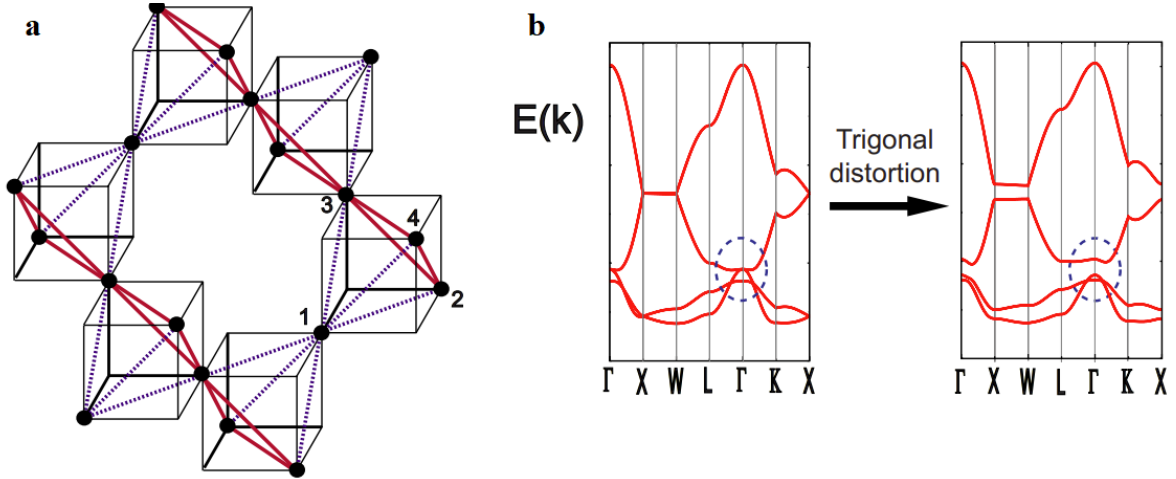


Figure 1.19 (a) Trigonal lattice of $\text{Pr}_2\text{Ir}_2\text{O}_7$ in $[111]$ direction (b) change of band structure induced by strain

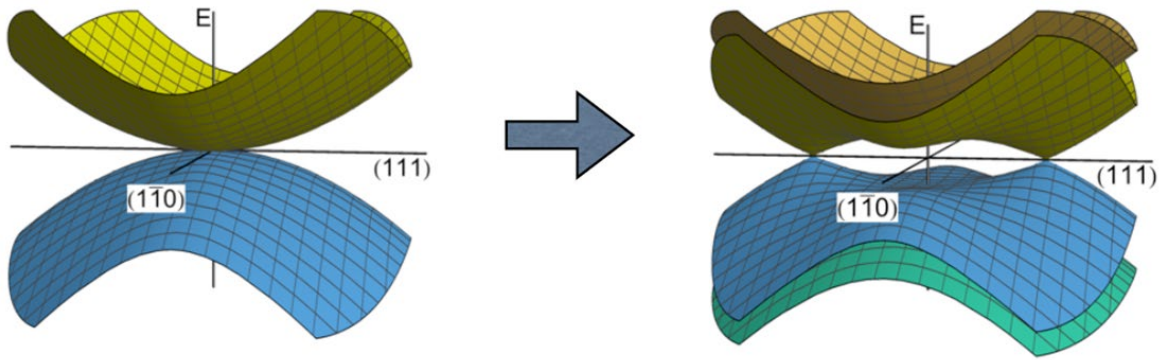


Figure 1.20 Weyl points generated from quadratic band touching by breaking symmetry

1.3. Purpose of the thesis

To enter a topological phase, breaking of cubic symmetry by applying strain is necessary for $\text{Pr}_2\text{Ir}_2\text{O}_7$. However, a strain of 1%, which is the lowest level to change electronic structure, is almost impossible to achieve in bulk. Additionally, as mentioned before, ARPES experiment requires a high-quality surface.

Besides, $\text{La}_2\text{Ir}_2\text{O}_7$ has larger A-site ionic radius, which is outside the range of Figure 1.16 and is expected to have similar but more obvious nontrivial electronic properties, yet this material cannot exist in stable bulk form. The only possible way to synthesize it is in the form of a 2-dimensional thin film where lattice strain can stabilize the phase.

For the reasons listed above, the purpose of this thesis is to find the best growth conditions for these two pyrochlore iridates with the aim of obtaining stoichiometric surfaces that might be suitable for an ARPES study. The technique used for growing the thin films is pulsed laser deposition.

Chapter 2. Methods

The experiment methods will be described in this chapter. The thin films were grown by Pulsed Laser Deposition (PLD). The ceramic targets used for PLD were either purchased from a commercial supplier or synthesized by Spark Plasma Sintering (SPS). The film surface morphology was studied by Atomic Force Microscopy (AFM). X-ray diffraction (XRD) was used for determining the phase composition of the film samples.

2.1. Thin film growth

A myriad of deposition techniques has been developed in the past decades to serve the needs of the microelectronics industry. Among the common methods of Chemical Vapor Deposition (CVD), Molecule Beams Epitaxy (MBE), Pulsed Laser Deposition (PLD), and Sputtering, PLD has various merits like good stoichiometry control and high deposition rate that make it particularly useful for oxide materials development.⁵¹ It is generally the preferred technique for growing complex oxide thin films owing to the ability of operating in the presence of reactive gases at pressure ranging from high vacuum conditions up to about 1 Torr.^{51–53}

The subject of thesis is the growth of the pyrochlore $\text{Pr}_2\text{Ir}_2\text{O}_7$ phase. Even though this family of pyrochlore iridates has numerous non-trivial properties, the growth of thin films is remarkably difficult. Most published works on iridate pyrochlores have turned to a special for PLD, known as solid-phase epitaxy (SPE), where an amorphous precursor film is grown by PLD at room temperature and the crystalline phase is obtained by annealing in a PLD chamber or in a furnace. Some of the predicted properties can be demonstrated in such films, but it is difficult to apply controlled strain by this technique and the films have a very poorly defined surface. For this reason, the most useful method for verifying the electronic structure, angle-resolved photoemission spectroscopy (ARPES), cannot be used. Strain analysis is also complicated in SPE films because strain only affects the substrate interface and a strong strain gradient may exist in the film. Both of these problems could in principle be solved by growing a crystalline film directly by PLD, but this still remains challenging due to the volatility of iridium oxides.

2.1.1. Pulsed laser deposition

PLD is a famous thin film growth technique for complex oxide film synthesis. The technique was developed for the synthesis of high- T_c cuprate superconductor thin films, notably the yttrium barium cuprate $\text{YBa}_2\text{Cu}_3\text{O}_{7-\delta}$ (YBCO) films⁵⁴. In recent years, it has been widely used to grow oxide heterostructures⁵⁵ because of the ability to form high-quality interface while working with many different oxide materials.

A typical PLD system is composed of a vacuum chamber and a pulsed laser system as shown in Figure 2.1. A bulk ceramic target is placed in front of the substrate inside the chamber. Light pulses from a high-power excimer or solid-state laser are focused on the surface of the target. Even for moderately low laser pulse energies of around 100 mJ, the temperature achieved near the focus point can reach several thousand degrees during the pulse time of a few nanoseconds, thereby evaporating a thin surface layer of the target material and generating a plasma plume that expands rapidly in vacuum. The plume shape, kinetic energy, and composition depend on the target material and the presence of a background gas in the chamber. When the plume reaches the surface of a heated substrate, the deposited adatoms migrate on the surface of the substrate and may form a crystalline phase if the deposition parameters are appropriate.

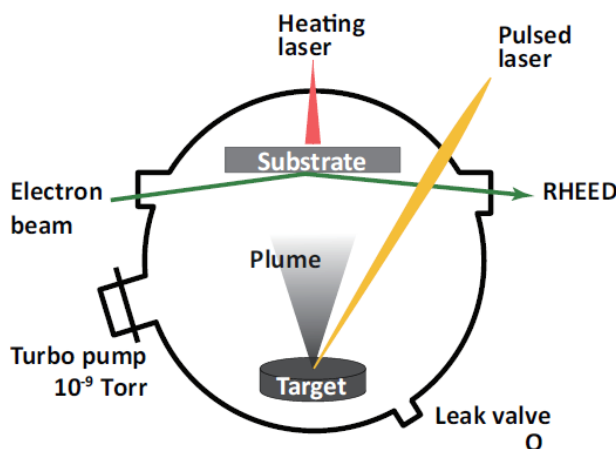


Figure 2.1 Schematic of a PLD chamber.

There are several process parameters that can be used to control the PLD process and the crystal phase formation. Some parameter ranges used in this work are shown below:

- a) Base vacuum: 10^{-9} Torr
- b) Background gas: O_2 , Ar, He
- c) Background pressure: $10^{-5} \sim 10^{-1}$ Torr
- d) Substrate temperature: $700 \sim 1000$ °C
- e) Laser fluence: ~ 1 J/cm²
- f) Laser pulse rate: 0.5~10 Hz

The substrate temperature was regulated by controlling the power of a continuous wave near-infrared semiconductor laser with a proportional–integral–derivative (PID) controller that obtained its feedback signal from an optical pyrometer. The crystal structure and composition vary depending on the substrate temperature. As a general guide, it is thus possible to use bulk phase diagrams to predict what would be a suitable growth temperature range. Besides the phase formation or decomposition, temperature can have a profound influence on the film surface morphology⁵⁶. Processes such as re-evaporation, nucleation and the formation of surface defects are all strongly related to the mobility of the deposited atoms. Temperature-

dependent surface migration rate changes are therefore commonly observed as different growth modes⁵⁷.

Both the composition and the pressure of a background gas can be controlled by valves connected to the main deposition chamber. Oxygen is usually filled as a background gas for oxide crystal growth, the pressure of which can affect the stoichiometry and the valence of cations⁵⁸; especially for elements like iridium that have volatile oxides, control of oxygen pressure is extraordinary critical. The ambient oxygen in a PLD chamber serves two purposes. In the vapor phase, when the ablated atoms collide with gas molecules, oxidizing reactions can occur and thermalizing collisions between the plume and the background gas reduces the kinetic energy of adatoms arriving at the substrate surface. The kinetic energy of adatoms affects the sticking coefficient (the likelihood that an atom remains on the surface instead of bouncing off), the migration length on the surface, and the probability of sputtering other atoms off the surface. The background gas also influences the surface through oxidizing reactions that occur between deposition pulses. Both gas-phase and surface reactions can have a significant impact on the crystallinity of the film. Figure 2.2 shows an example of SrRuO₃/BaTiO₃ heterostructure thin films grown in different background gas environments.

As an essential part of PLD, the ablation laser parameters must be chosen suitably. Considering light absorption in bulk PLD targets, there are variety of lasers that can be used for ablating different materials with laser operating at different wavelengths.⁵⁹ Since oxide materials can have very large band gaps, it is easier to ablate many oxide with a deep UV laser, such as a KrF excimer laser. The operating wavelength is 248 nm, which corresponds to a photon energy of 5 eV. For evaporating metals or organic materials, a near-infrared Nd-YAG laser working at 1064 nm might be used instead. In this work, all films were grown with KrF excimer laser ablation.

For a specific target material, a plasma plume can be generated only if the fluence of the laser reaches a certain threshold value. The fluence, or energy density, value also depends on the laser pulse length. Since the pulse length is fixed for a given laser, it is usually sufficient to specify the type of laser and the energy density, which is easy to measure with a pyroelectric energy sensor.

Working very close to the ablation threshold energy, severe stoichiometry variations may occur in the plume, since some elements may be preferentially ablated. Too high fluence will increase the kinetic energy of the atoms in the ablation plume to a point where adatoms impinging on the film surface may start to re-sputter the film material, leading to degraded film quality.⁶⁰ The crystallinity reduction is often visible in X-ray diffraction patterns as a shift of the film lattice parameter. Figure 2.3 shows the lattice constants of SrTiO₃ thin films grown at different laser fluences. A near-zero expansion can be achieved in a very narrow fluence range close to 0.3 J/cm² due to the exact matching of the Sr/Ti ratio in the plume at that laser energy density. The fluence can be tuned by adjusting the laser pulse energy, attenuating the beam intensity with optical attenuators, and by adjusting the distance of the focus lens from the surface of the target. It is thus possible to adjust independently the ablation area and the energy density.

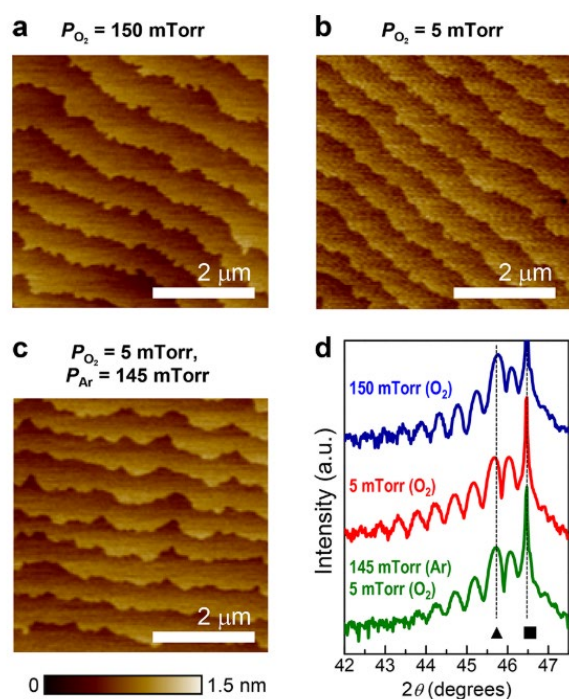


Figure 2.3 Structural characterizations of SrRuO₃/BaTiO₃ heterostructures.⁸ (a-c) AFM images of three films grown in different background gas conditions and (d) XRD 2θ - ω scans of the SrRuO₃/BaTiO₃ heterostructures.

Another important parameter is the ablation pulse rate. The general frequency range for oxide growth is 1 Hz to 10 Hz. The pulse rate mainly affects the film growth mode since the time interval between deposition pulses allows the surface atoms to migrate. The pulse interval also affects the oxidation of the film, which is generally a slow process. Even for a fractional unit cell layer, the oxidation process may take seconds to minutes.⁶¹ In this work, the pulse interval is a particularly important parameter, as the oxidation of iridium can lead to the formation of volatile iridium oxide phases that rapidly evaporate from the film surface. The ablation pulse rate thus also affects the iridate film composition.

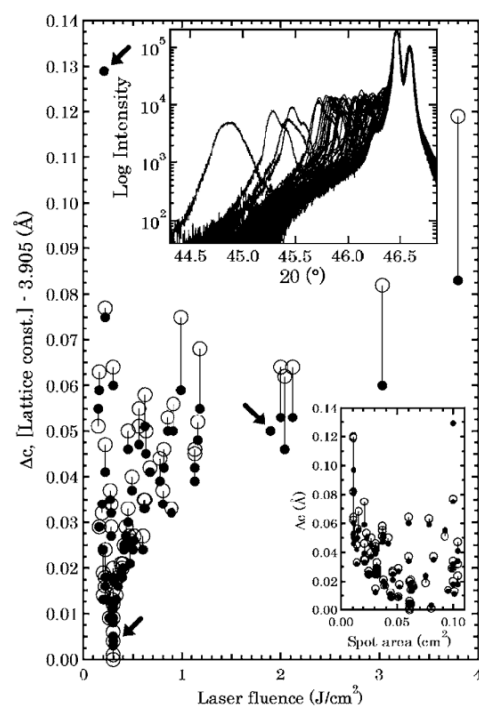


Figure 2.3 Expansion of the film lattice constant as a function of laser fluence.

2.1.2. Solid-phase Epitaxy

When high-temperature growth of materials containing volatile elements is needed, it is possible to use solid-phase epitaxy. The SPE process can be divided into two steps. In the first step deposition at a low temperature is used to form a metastable amorphous layer on a crystalline substrate. Volatility problems can be avoided due to the low growth temperature, but the advantage of stoichiometric evaporation in PLD can still be used to obtain an amorphous precursor film that has the correct cation ratio. In the second step, the amorphous film is annealed to reorder atoms and form a crystalline phase. If the bulk diffusion rate of a volatile species is low, it is possible to obtain a crystalline film while volatility-related stoichiometry changes are limited to the film surface, even if the crystallization is done at high temperature.⁶² In practice, crystallization usually starts at the substrate interface and an epitaxial film is obtained. However, it is difficult to control strain or grain size, and the surface quality cannot be maintained. Figure 2.4 shows how the crystallization process occurs in the growth of a germanium thin film.

There are two common methods for the first step of SPE: high-fluence ion implantation and film deposition. Here, only film deposition method will be discussed. Compared to epitaxial film deposition, usually a much lower substrate temperature is used amorphous layer growth to prevent crystallization, evaporation, and re-sputtering. Because of the mild growth conditions, stoichiometry can be preserved, especially for the highly volatile elements.

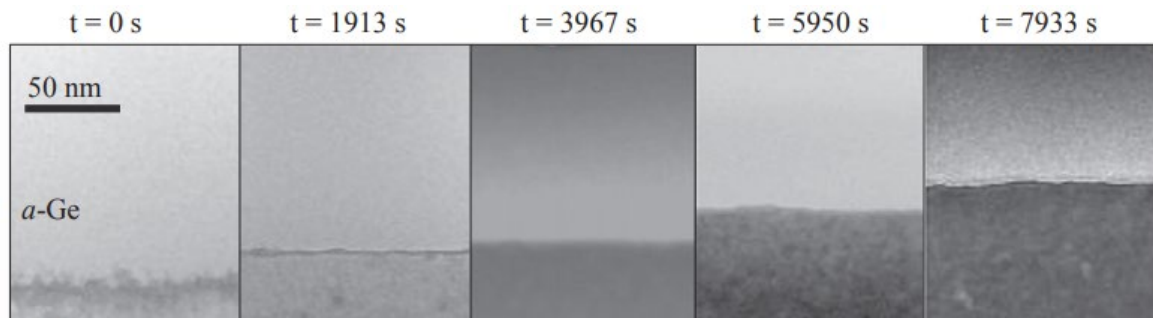


Figure 2.4 Cross-section transmission electron microscope images taken at various time points of Ge crystallization.

Various methods can be used to heat the sample including a conventional box furnace or in-situ annealing in a deposition chamber. The heating rate can be used to control the grain formation and strain relaxation in the film.

Although many attempts to grow iridate pyrochlores by SPE have been reported^{63–68}, some difficulties still remain unsolved. For conventional SPE, Gallagher et al. successfully grew a pyrochlore iridate $\text{Nd}_2\text{Ir}_2\text{O}_7$ film in 2016.⁶⁸ The reported STEM image shows good crystallinity but a disordered substrate-film interface is also evident in Figure 2.5. Due to the interface defects, the film is fully relaxed as shown by the XRD measurements. Very recently, Kim et al. reported a new SPE technique called repeated rapid high-temperature synthesis epitaxy (RRHSE),⁶⁶ which allowed them to obtain a fully epitaxial $\text{Nd}_2\text{Ir}_2\text{O}_7$ film. However, synthesis of an iridate pyrochlore film with a well-ordered and stoichiometric surface is still eagerly anticipated.

2.2. Target synthesis

One of the great benefits of PLD is the ability of a high-fluence laser to ablate any material, even materials with very high melting points. However, the increase of ablation laser fluence comes at a cost of generating large, up to micron-scale particles in the ablation process. The characteristics of the ablation target, especially the density but also the stoichiometry affect the surface melting and particle generation, and thus also the film quality⁶⁹. A soft target or a low-density ceramic target can be easily damaged by a high-fluence laser, thus generate big particles on the film, which dramatically lowers the quality of film and hinders surface analysis. Figure 2.6 shows a high-speed camera image of a PLD target taken a few microseconds after the plasma plume has expanded into vacuum. Bright streaks can be seen above the target surface. These streaks are hot light-emitting particles ejected from the target surface by the ablation laser. Particles ejected from a target coat the surface of the film and can be seen easily under an optical microscope (Figure 2.6b). In some cases the particle generation can be reduced by periodically polishing the target surface.

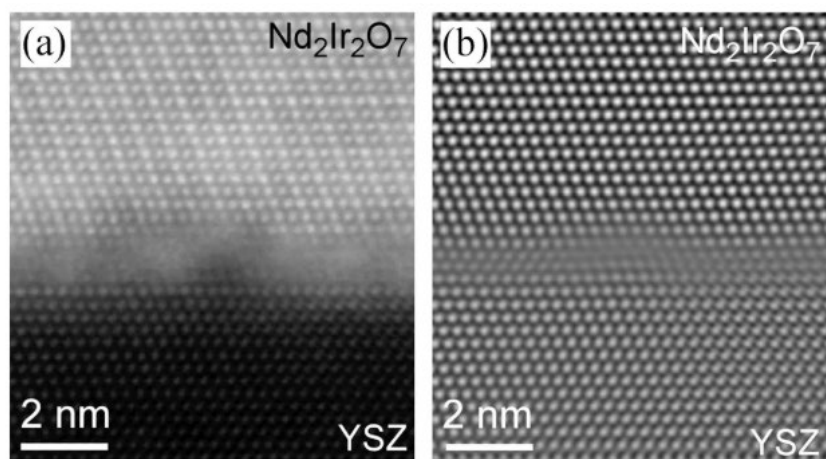


Figure 2.5 Raw STEM image (a) and a Fourier-filtered reconstruction (b) of a $\text{Nd}_2\text{Ir}_2\text{O}_7$ film grown on a YSZ (111) substrate.

Common targets for PLD such as SrTiO_3 or TiO_2 can be directly purchased from ceramics suppliers. While commercial targets have excellent density, it is not possible to purchase less common compositions, such as $\text{Pr}_2\text{Ir}_2\text{O}_7$. For these special requirements, most groups have used solid-state reaction methods, usually sintering within a quartz tube, to synthesize the target phase in bulk powder form. Then powders can then be ground, pressed, and sintered again to prepare a ceramic pellet for PLD use. However, if the final phase is already fully formed in the bulk powder synthesis step, the pressing and sintering produced a target with a density of only about 50% because no further reaction takes place in the pellet sintering stage. Such targets cannot be used for fabricating high-quality thin films.

Due to the volatility of Ir oxides, in this work there is little relation between the target stoichiometry and film stoichiometry. Firstly, iridium may be lost from the film surface due to evaporation of an oxide. It may thus be necessary to use an Ir-rich target to correct for this stoichiometry change. Secondly, stable Ir oxide, IrO_2 , can be easily reduced back to metal at high temperature. This process can happen on the target surface during repeated ablation if there is significant thermal energy transfer from the laser pulse to the target surface. In practical PLD use of a pure IrO_2 target, for example, the black oxide surface gradually turns metallic gray due to the reduction of the oxide to a metal. If the same process occurs in a $\text{Pr}_2\text{Ir}_2\text{O}_7$ target, the target surface gradually becomes strongly Ir rich and PrO_x is preferentially ablated instead. Many research groups in this field have tried to compensate for the iridium loss through different ways, among which to synthesize an iridium-rich target is the most common way. In this sense, solid-state reaction of a $\text{Pr}_2\text{Ir}_2\text{O}_7$ phase prior to pressing and sintering a target pellet is not necessary. Instead, the hardness of the target is more critical. In this work, a spark plasma sintering (SPS) machine was used to prepare a high-density target using a simple mixture of binary oxide powders (Pr_6O_{11} , IrO_2 , or La_2O_3) directly.

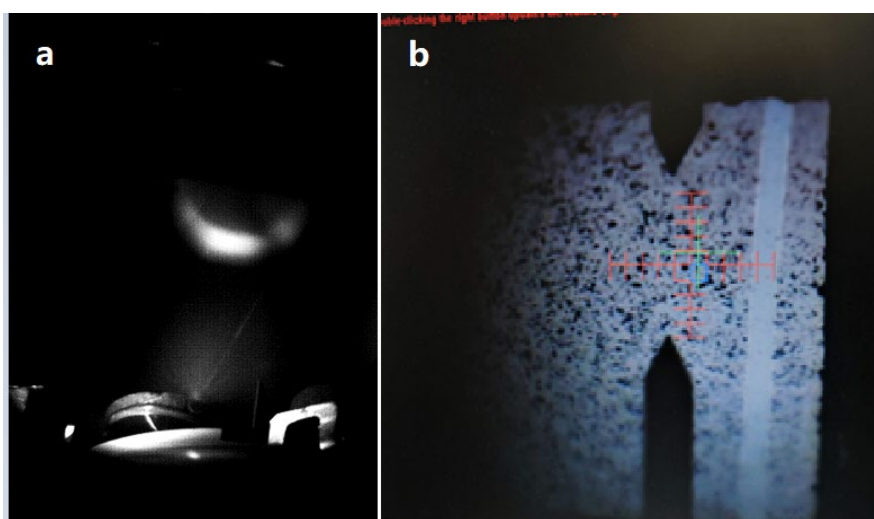


Figure 2.6 (a) CCD image of particles generated from a target just after an ablation pulse. (b) Microscopic image of a contaminated thin film surface.

Compared to conventional furnace sintering methods, SPS provides an extremely high heating rate, reducing the sintering time from hours or days to minutes⁷⁰. Besides, it can sinter

a denser material with a well-preserved nanostructure. A typical SPS machine consists of vacuum chamber, uniaxial hydraulic press, electrodes, DC pulses generator and a series of sensors as shown in Figure 2.7. Ground powders were put inside a graphite die with two graphite punches. A pressure of 100 MPa was applied while pulsed current of up to 10 kA were applied to the powder and die through the punches.

In this work, graphite punches with a diameter of 15 mm were pressed at 17.4 kN to achieve 100 MPa pressure. The SPS chamber was pumped to vacuum, flushed with argon several times, and the sintering was done in an argon atmosphere. After 15 minutes of heating from room temperature with a heating rate of about 60°/min, powders were sintered at 900°C for 10 minutes. Figure 2.8 shows the profile and photograph of the SPS.

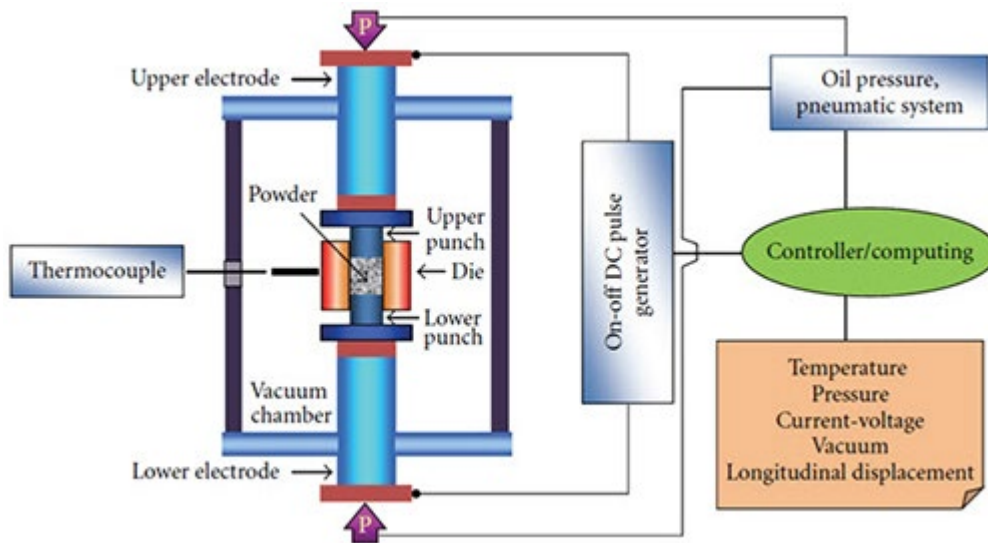


Figure 2.7 Schematic image of SPS

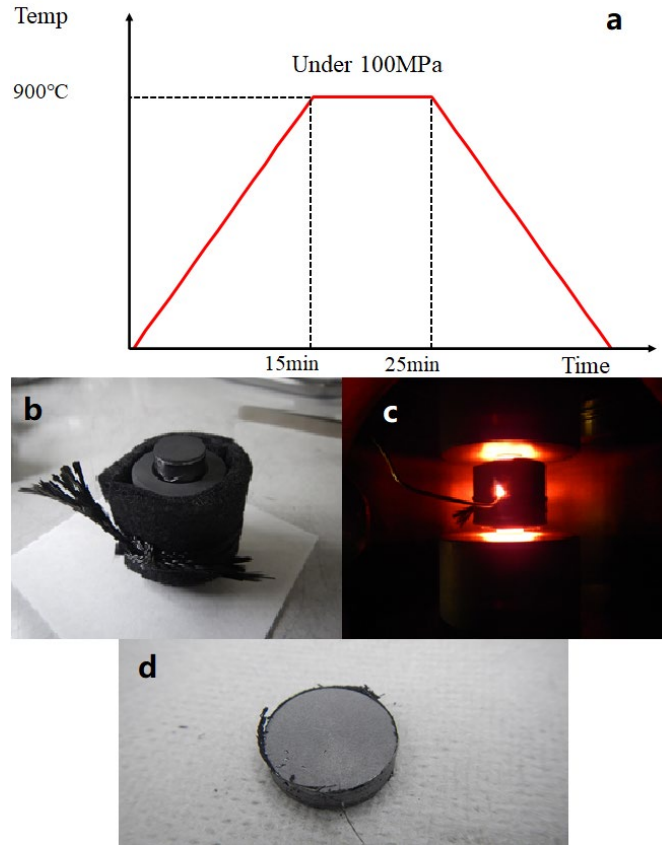


Figure 2.8 (a) Temperature profile of SPS processing. Preparation (b) and sintering (c) of graphite punches and die (powders inside). (d) Final target got obtained from SPS.

2.3. Characterization

2.3.1. Atomic force microscope

AFM is a widely used technique in surface analysis, which is regarded as a milestone in the history of nano science since it was invented in 1986⁷¹. Compared with scanning tunneling microscope (STM), which is another famous technique in the same scanning probe microscope (SPM) family, AFM can be utilized in a much wider range including physics, chemistry, biology and medicine in that it doesn't need a conductive surface.

In general, AFM detects the nano structure by transforming the interaction force between a sharp tip and sample surface into a cantilever-tip transducer⁷² as shown in Figure 2.9. The elastic cantilever follows Hooke law and is highly sensitive to tiny force. When tip is close to the sample surface, a small atomic force will be generated, which can be obtained by measuring the elastic deformation. Elastic deformation is measured by an optical system where a laser beam is focused at the end of the cantilever and reflected to a detector. Signal of detector changes with the bending of cantilever, from which deformation can be calculated as well as the atomic force. There are several formulations to describe relation between atomic force and distance in different situations.

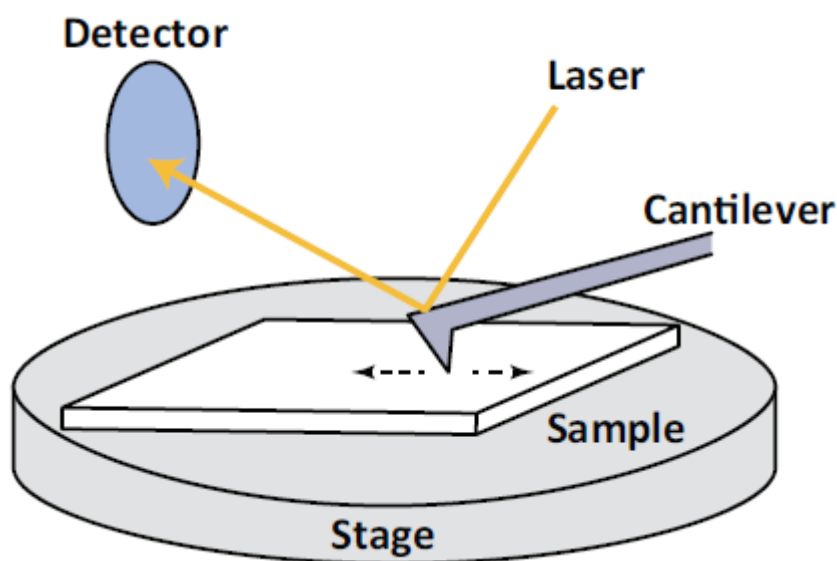


Figure 2.9 Schematic image of AFM

The most common working mode is Constant Force Mode, which keeps the deformation of cantilever constant and records the trace of tip's movement. In this mode, a feedback loop is employed, whereas the scanning speed is lowered. There is another mode available to provide a higher scanning speed called Constant Height Mode, which sacrifices the feedback loop and usually uses for smooth surface. The distance between tip and sample surface is kept constant in this mode. Surface morphology is imaged by the deformation change.

To prevent from damaging the sample surface, AFM can also measure long-range force like electrostatic force and Van der Waals force using a Non-Contact Mode. Besides, resonance can be applied to the cantilever to reduce the friction and strain using a tapping mode.

2.3.2. X-ray diffraction

XRD has been one of the most important technique in the study of crystallinity for century. A typical x-ray equipment consists of x-ray generator, detector and sample stage, along with several optional fittings. For thin film measurement, a so-called 4-circle XRD (Philips; X'Pert-

MRD) was utilized (Figure 2.10(a)). The lattice parameter is obtained by applying a $2\theta/\theta$ scan. From the diffraction angle, the interplanar distance can be calculated by the Bragg's law⁷³:

$$2d_{hkl} \sin \theta = n\lambda,$$

where d_{hkl} denotes the interplanar distance, λ is the wavelength of x-ray (Figure 2.10(b)). In this experiment, Cu is selected as the x-ray source, which has wavelengths of Cu $K_{\alpha 1} = 1.54054 \text{ \AA}$ and Cu $K_{\alpha 2} = 1.54432 \text{ \AA}$. For cubic system, lattice parameter can be calculated from the following formula:

$$d_{hkl} = \frac{a}{\sqrt{h^2 + k^2 + l^2}},$$

where a denotes the lattice parameter.

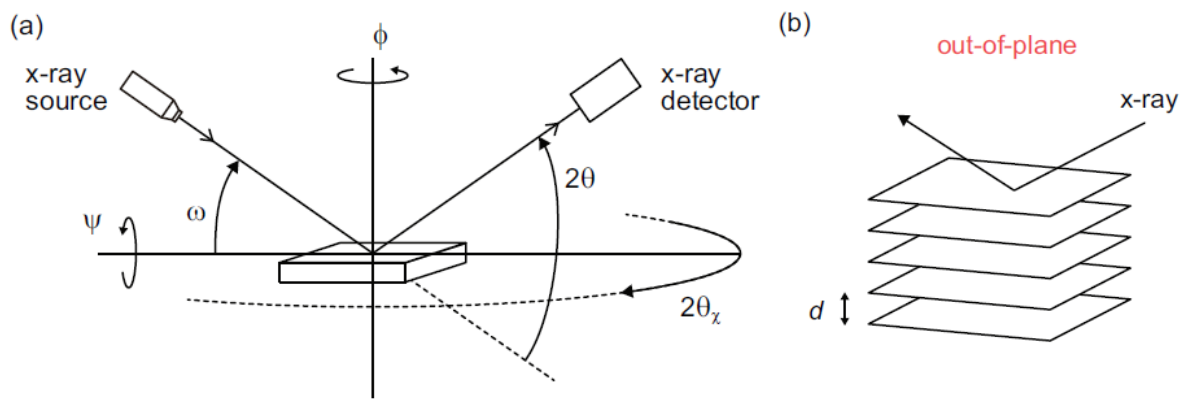


Figure 2.10 (a) Schematic image of a 4-circle XRD (b) Out-of-plane x-ray diffraction

Different from conventional powder XRD, thin film is limited in thickness, which cause some special properties. Usually, the film peaks are much broader than then substrate peak in that x-rays are diffracted over a wide angle in thin layer. Besides, if a film is well-grown, the thickness fringes can be observed in XRD measurement (Figure 2.11), which are created by the phase difference between different surface and are inversely proportional to the thickness.

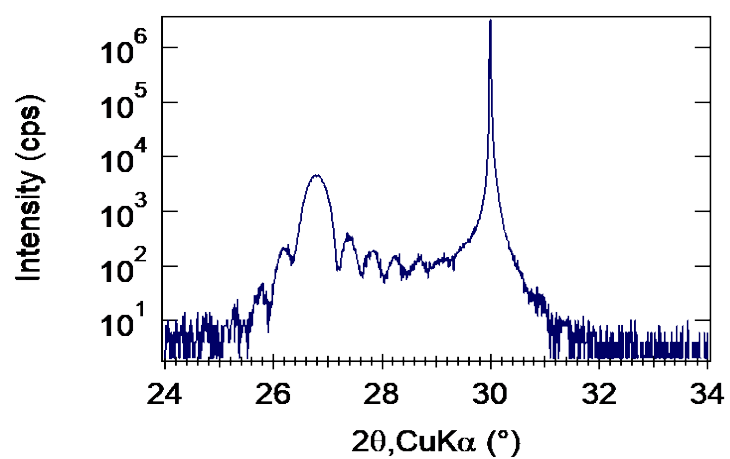


Figure 2.11 An example of thickness fringe in XRD, where the highest peak demotes substrate.

Chapter 3. Growth of $R_2Ir_2O_7$ ($R = Pr, La$)

3.1. Substrate

A single crystal substrate is the most important part in the growth of an epitaxial thin film. Even for the same film material, different substrates can be utilized for different applications. There are numerous aspects that need to be considered in the selection of a substrate, including chemical compatibility, lattice matching, thermal expansion match and thermal stability, etc.

In this work, yttria-stabilized zirconia (YSZ) substrates with a (111) surface orientation were used. The amount of Y_2O_3 , which is added to ZrO_2 to stabilize the cubic structure at room temperature, can vary by manufacturer. The crystal parameters of the YSZ(111) substrates provided by Shinkosha are shown in Table 3.1. The cubic stability and small lattice mismatch of about 1.12% with $Pr_2Ir_2O_7$ (10.394\AA) make a near-perfect platform for the growth of epitaxial pyrochlore films. Additionally, YSZ is an excellent insulator, which is helpful for transport analysis of thin films. Inducing epitaxial strain in thin films is one of the purposes of

Composition	$Y_2O_3(10 \text{ mol\%})-ZrO_2(90 \text{ mol\%})$
Crystal system	Cubic
Crystal structure	CaF_2
Lattice constant	$a=0.5139 \text{ nm}$
Melting point	$2500 \text{ }^\circ\text{C}$
Density	$6.05 \text{ g/cm}^3(20 \text{ }^\circ\text{C})$
Dielectric constant	27
Thermal expansion coefficient	$10.3 \times 10^{-6}/^\circ\text{C}$

Table 3.1 Properties of YSZ manufactured by Shinkosha

this work, which can be done naturally by the lattice mismatch and different strain level can be obtained by adjusting the yttria ratio in YSZ or by using suitable buffer layers.

To grow well-ordered thin films with atomically flat surfaces, the substrate surface has to be of equal or better quality. For YSZ(111), excellent surfaces can be obtained by annealing polished crystals at 1250°C for 2 hours in a box furnace in air. A clear step-and-terrace surface forms during the annealing. Figure 3.1 shows AFM images of the surface of a YSZ(111) substrate before and after annealing. The step height is 0.36nm, corresponding to the distance between two atomic layers.

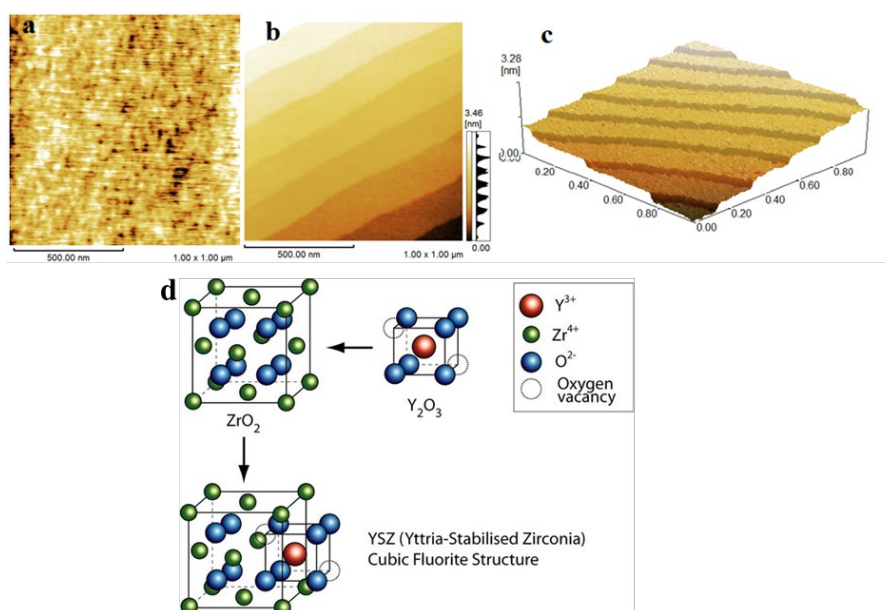


Figure 3.1 AFM images of the YSZ(111) surface (a) before annealing and (b) after annealing. (c) 3D rendering of the annealed surface shown in (b). (d) crystal structure of YSZ

3.2. Growth of $\text{Pr}_2\text{Ir}_2\text{O}_7$

3.2.1. Deposition with a solid-state reaction target

The film growth and phase formation is affected by several deposition process parameters. As with any film process development, several mapping experiments are necessary to find a suitable process parameter range for detailed study. In this case, the initial mapping was done with a stoichiometric $\text{Pr}_2\text{Ir}_2\text{O}_7$ target made by solid state reaction. The PLD pulse laser rate was 2Hz, the oxygen pressure range was 0.3 mTorr to 3 mTorr, and the substrate temperature was

fixed at 1000°C, which is close to the bulk single crystal synthesis conditions of $\text{Pr}_2\text{Ir}_2\text{O}_7$ ⁷⁴. XRD $\theta/2\theta$ scans were used for identifying the composition of these films.

Figure 3.2(a) shows narrow XRD scans of films deposited at different oxygen pressures and a fixed substrate temperature of 1000°C. The highest peak that is marked with an asterisk is the YSZ substrate peak. The expected diffraction peak position of bulk $\text{Pr}_2\text{Ir}_2\text{O}_7$ is obtained from the Powder Diffraction File (PDF) database and marked with a vertical dashed line. Only the film deposited at 0.3 mTorr pressure showed the presence of a pyrochlore diffraction peak near the dashed line. This peak cannot be seen if the oxygen pressure is increased even slightly. Besides the pyrochlore peak, all films show several other diffraction peaks on the left-hand low-angle side. These peaks appear to belong to various non-stoichiometric praseodymium oxide phases (Pr_xO_y), most of which have not been studied in detail and do not appear in the PDF database.

For more information, an XRD wide-area scan of the pyrochlore film was performed as shown in Figure 3.2(b). Two peaks with high intensities at 40.7° and 88.1° indicate that iridium metal segregated as a secondary phase in this film, which has a strong influence on the electronic measurements. Moreover, clear peaks appear for even (*hll*) index positions of $\text{Pr}_2\text{Ir}_2\text{O}_7$, which corresponds to a defect-fluorite structure with half the expected pyrochlore

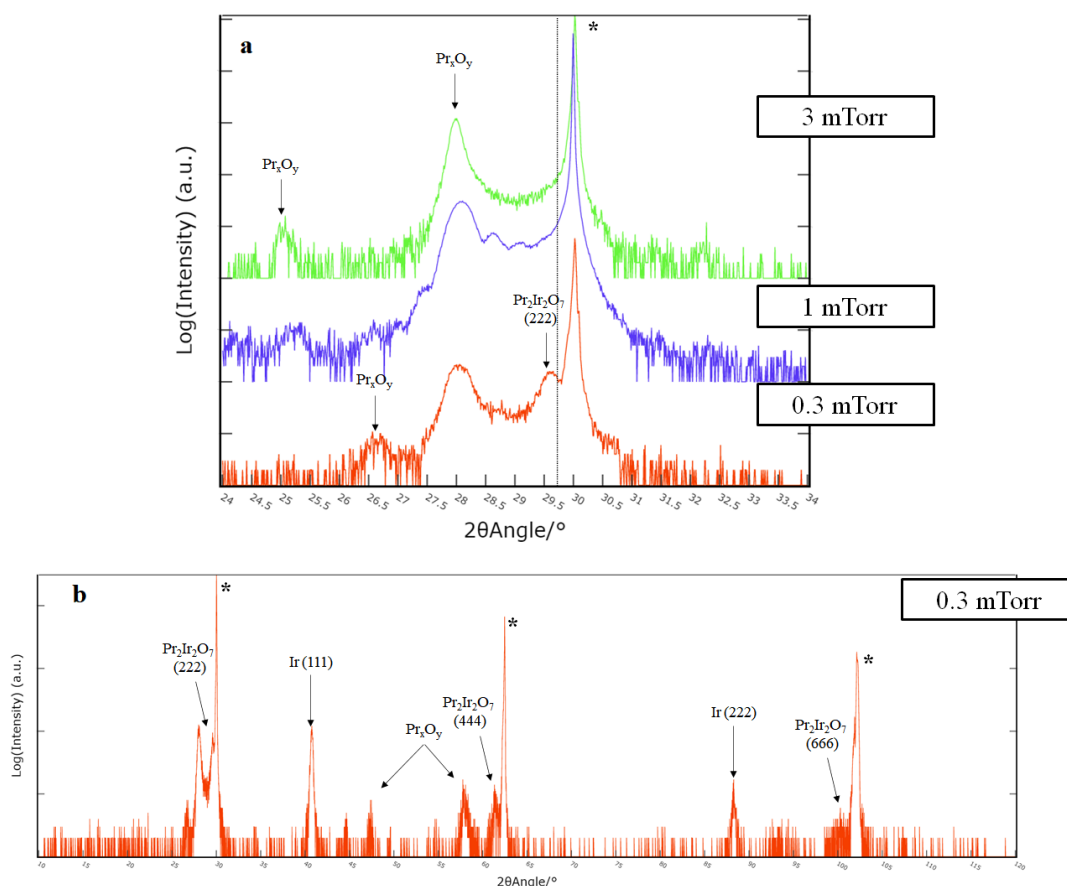


Figure 3.2 XRD narrow-area scans (a) and a wide-area scan (b) of $\text{Pr}_2\text{Ir}_2\text{O}_7$ grown at a substrate temperature of 1000°C at different oxygen pressures.

lattice parameter, as shown in Figure 3.3⁷⁵. In the defect fluorite structure, the A^{3+} and B^{4+} cations are distributed randomly, and there is no difference in oxygen sites. This structure is usually induced by extreme environment conditions such as high temperature, high pressure, or irradiation⁷⁶.

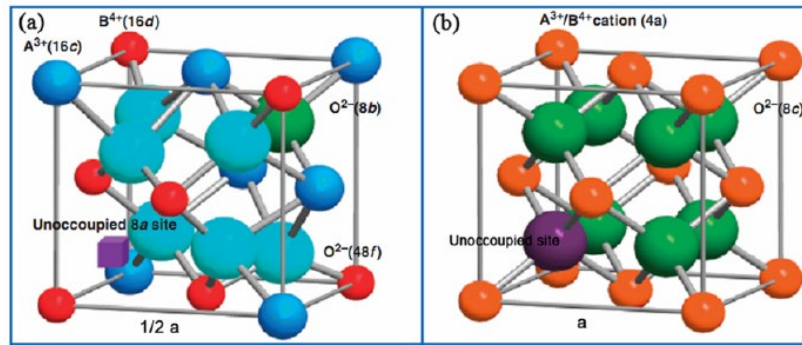


Figure 3.3 Crystal structure of (a) 1/8 of unit cell of pyrochlore and (b) defect-fluorite

Since the reason for the formation of the iridium metal and defect-fluorite may be related to the high substrate temperature, a lower substrate temperature was applied, as shown in Figure 3.4. Narrow scans show that the defect-fluorite phase disappears when the growth temperature is reduced by just 50°C, while a strong iridium metal peak remains in the wide scans. Besides, several depositions were done in this region and the results are shown in Figure 3.5. This indicates that there is only an extremely narrow growth window for $\text{Pr}_2\text{Ir}_2\text{O}_7$ at high temperature and low oxygen pressure, while this condition is also advantageous for the formation of segregated iridium metal. The iridium metal peaks disappear with the increase of oxygen pressure, which can be explained by the strongly volatile behavior of iridium oxides, IrO_3 in particular. Moreover, the upper limit of temperature comes from the decomposition temperature of $\text{Pr}_2\text{Ir}_2\text{O}_7$, which is about 1100°C⁶⁴.

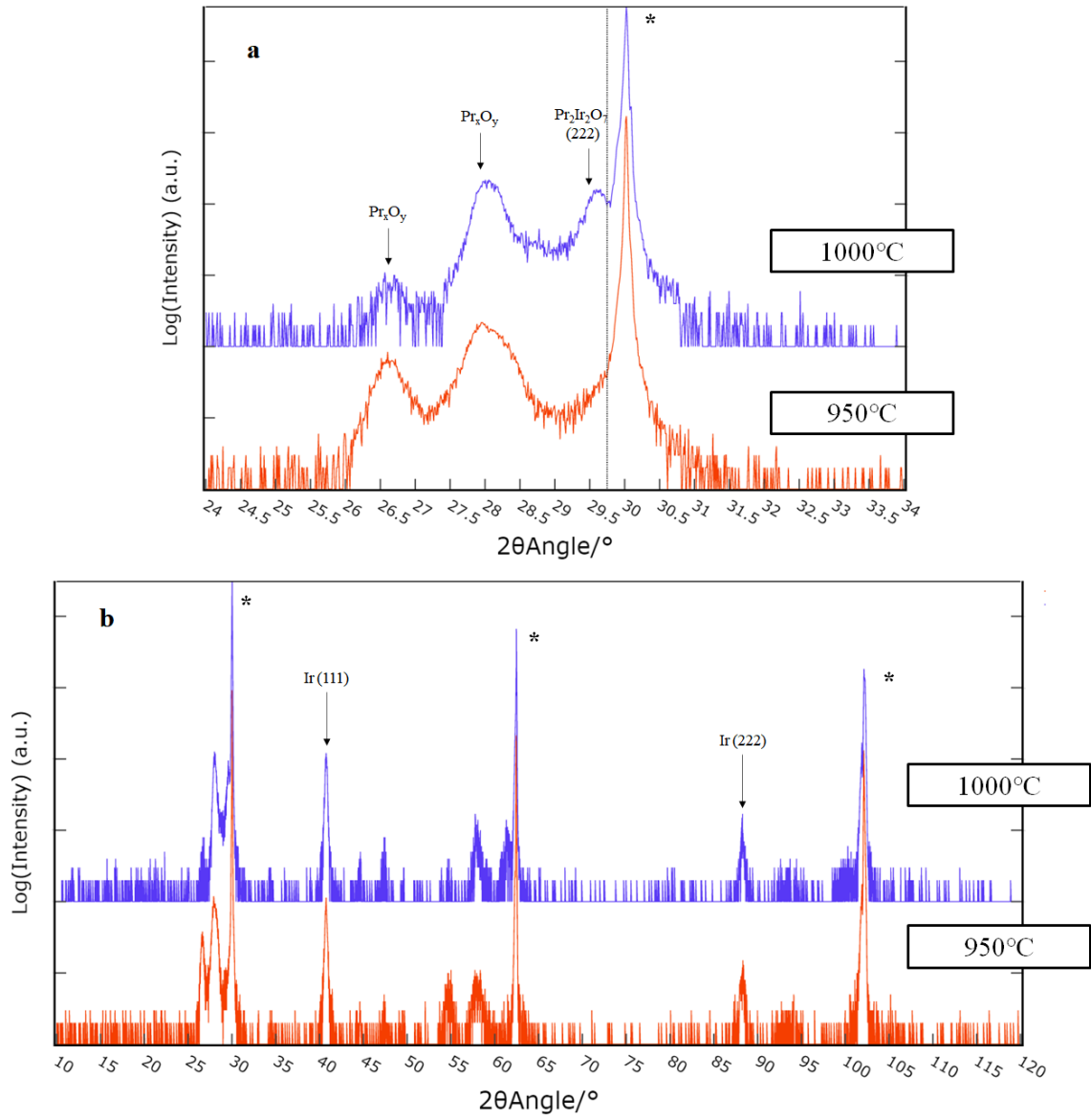


Figure 3.4 XRD narrow scans (a) and wide scan (b) of $\text{Pr}_2\text{Ir}_2\text{O}_7$ films grown at different substrate temperatures at 0.3 mTorr oxygen pressure.

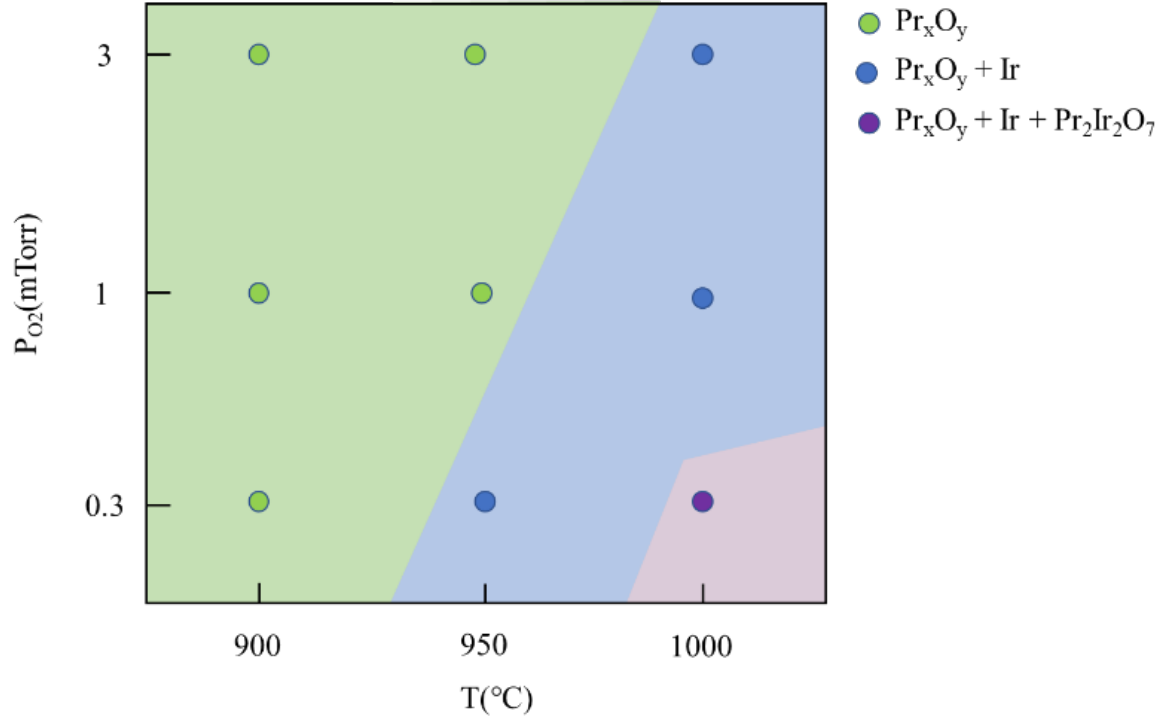


Figure 3.5 Phase diagram of $\text{Pr}_2\text{Ir}_2\text{O}_7$ films grown on YSZ(111) substrates.

Additionally, numerous particles were found on the surface of these films, which strongly hinder the surface characterization and may have influence on the composition characterization, as shown in an optical micrograph in Figure 3.6a (the light masking line width on the right-hand edge of the micrograph has a width of about 0.3 mm). The presence of particles on the film surface can be ascribed to the low density of the pressed target pellet, which leads to the ejection of large particles from the target during laser ablation. Figure 3.6b shows a photograph of a strongly damaged target surface after prolonged irradiation with a high-fluence laser. For more details, a high-speed CCD camera was set to capture images a few hundred ns after the luminous ablation plasma plume had dissipated. The image in Fig. 3.6c shows bright lines emanating from the target surface. These are tracks of hot micron-scale particles being ejected from the target surface. Since the velocity of the macroscopic particles is much lower than the plume, these tracks can be seen after the plume has passed.

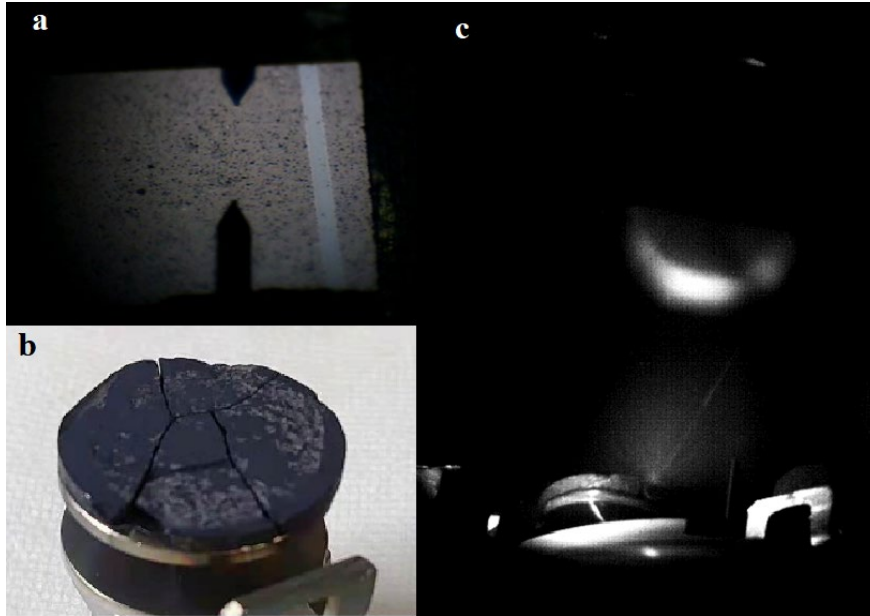


Figure 3.6 (a) Photograph of particle-contaminated film surface. (b) Damaged target surface. (c) CCD image of particles being ejected from the target.

3.2.2. Depositions with spark plasma sintering target

Deposition experiments done with stoichiometric targets containing a pre-reacted bulk $\text{Pr}_2\text{Ir}_2\text{O}_7$ powder indicated that the film composition deviates strongly from the target due to the segregation of Ir metal or various Pr oxides. One of the main benefits of PLD, namely stoichiometric transfer of material from a target to a film, cannot be relied on for iridate film growth. It thus appeared that it is not necessary to prepare a stoichiometric bulk powder target at all and it may instead be possible to simply use a mixture of two unreacted oxides in a compressed target pellet. The advantage of this approach is that it is easy to prepare targets with various Pr:Ir ratios, that is not possible for stoichiometric bulk synthesis.

Spark Plasma Sintering (SPS) was used to prepare sintered harder targets (Section 2.2). Since the volatility of iridium is conventionally regarded as the biggest challenge in the growth of iridates, more IrO_2 powder was used to make a target with a molar ratio of Pr: Ir = 1: 3. Compared with the previous target, this target can endure 3 times higher fluence without producing particles. However, the irradiated region on the surface of this target rapidly turned light gray during ablation, which is considered to be due to the formation of an iridium-rich surface layer due to the preferential evaporation of Pr oxides. A similar problem occurs for the stoichiometric targets and it can be mitigated by periodically polishing the target surface.

Firstly, a similar mapping at different oxygen pressure was done with the new target while the substrate temperature was fixed at 1000°C. Figure 3.7 shows the XRD results. From the narrow scan, a weak pyrochlore peak could only be obtained at 0.05 mTorr, which is 6 times lower than the optima oxygen pressure for growth from a stoichiometric target. Moreover, these films showed a much richer variety of praseodymium oxide phases, which are strongly affected by the oxygen pressure. A wide XRD scan shows a decreasing iridium metal peak with the increase of oxygen pressure. In general, films grown using this target are more sensitive to oxygen pressure. The reason may be that this target contains more oxygen. Oxygen in the target will be released as plasma when irradiated by a laser, which is much more reactive than the background molecular oxygen gas.

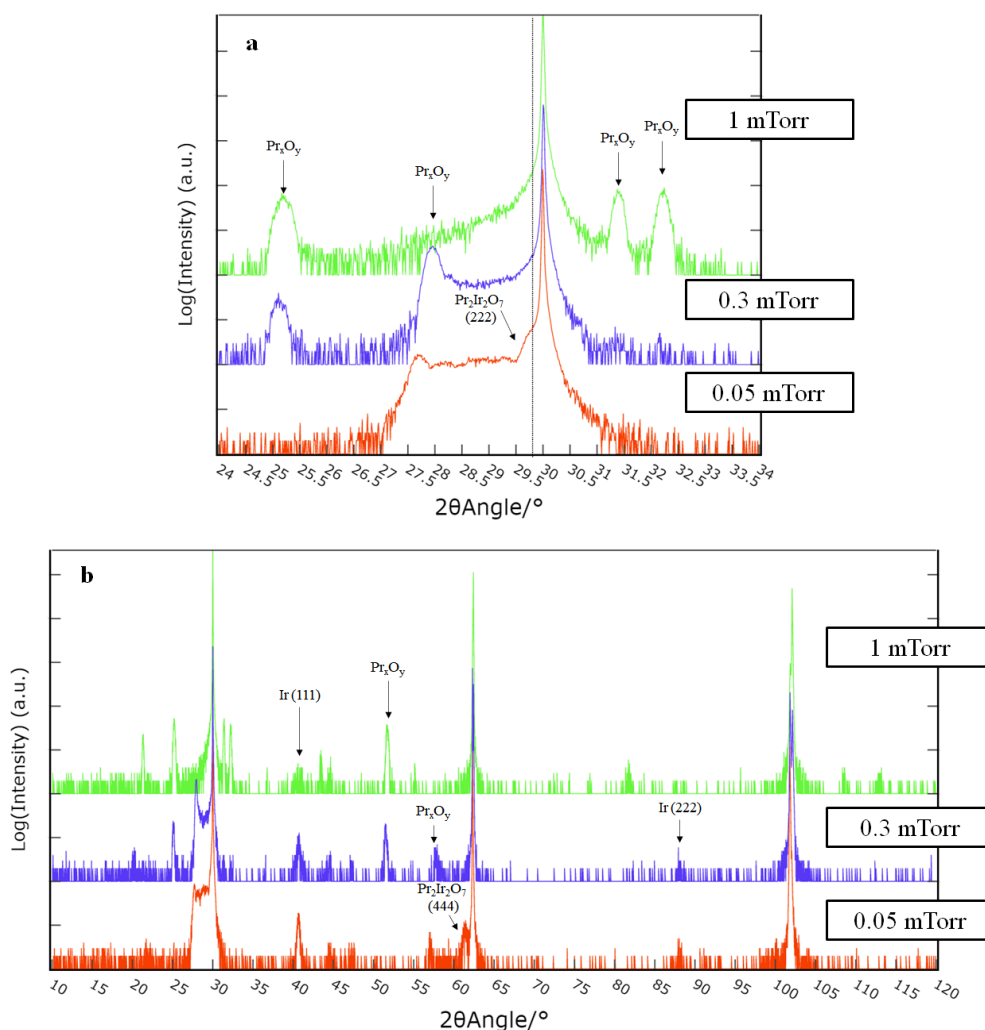


Figure 3.7 XRD narrow-area scans (a) and a wide-area scan(b) of $\text{Pr}_2\text{Ir}_2\text{O}_7$ grown at a substrate temperature of 1000°C at different oxygen pressures using a mixed-oxide target.

This iridate film was then annealed in air at 1000°C for an hour in a box furnace, and the surface was characterized by AFM. Figure 3.8 shows the AFM images of the film before and after annealing. Before annealing, the islands on the surface were triangular and separate, which may be due to the iridium metal behavior⁷⁷, while more extended islands appeared after annealing. The XRD results are shown in Figure 3.9. The iridate pyrochlore phase disappeared

after annealing, while new praseodymium oxide phases were formed. this behavior is quite different from previous films. Moreover, wide scans show that a sharp iridium metal peak remained after annealing, which indicates that iridium metal in this film is stable and did not oxidize even when annealed in air.

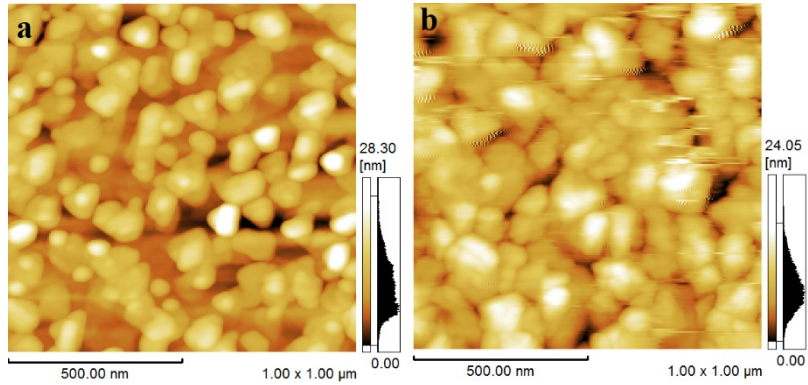


Figure 3.8 AFM images of $\text{Pr}_2\text{Ir}_2\text{O}_7$ films (a) before annealing and (b) after annealing.

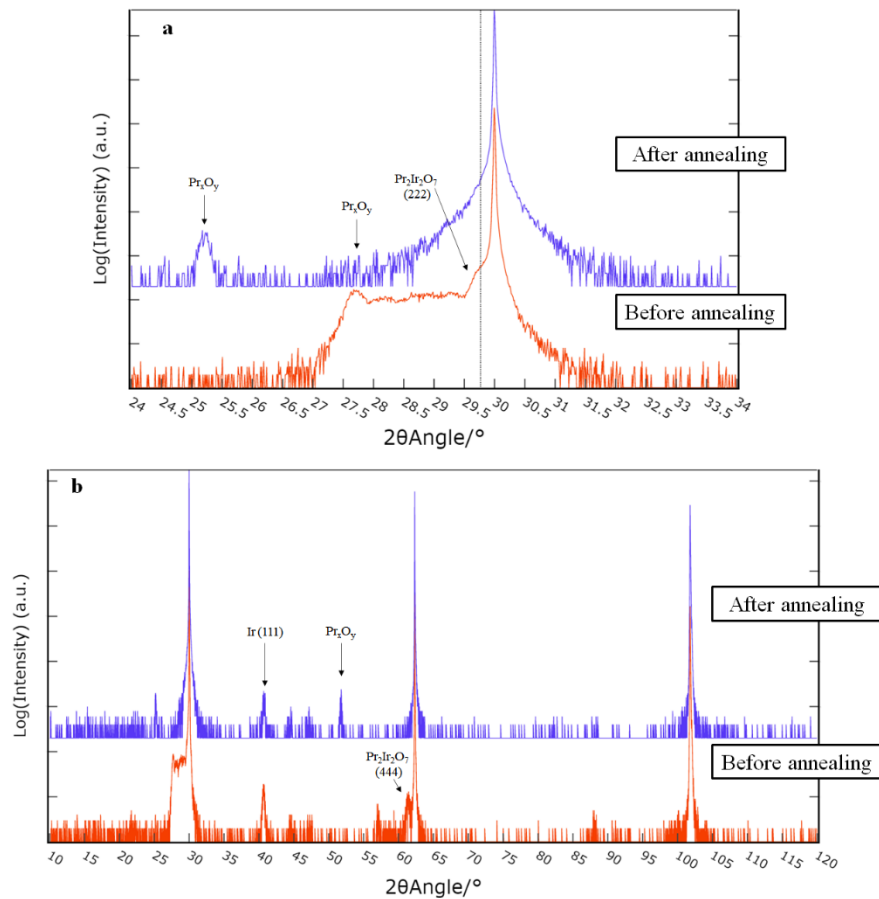


Figure 3.9 XRD narrow-area scan(a) and wide-area scan(b) of $\text{Pr}_2\text{Ir}_2\text{O}_7$ film before and after annealing.

Since this SPS target had the ability to endure high laser fluences, the fluence dependence was also investigated at a substrate temperature of 1000°C and oxygen pressure $P_{O_2} = 0.05\text{mTorr}$, as shown in Figure 3.10. The iridate pyrochlore phase only appeared in the film deposited using the highest laser pulse energy, while no iridium metal could be detected in the films grown at lower laser pulse energies (Figure 3.10 insert). This indicates that high fluence is necessary for the formation of the iridate pyrochlore phase, but this also leads to the segregation of Ir metal.

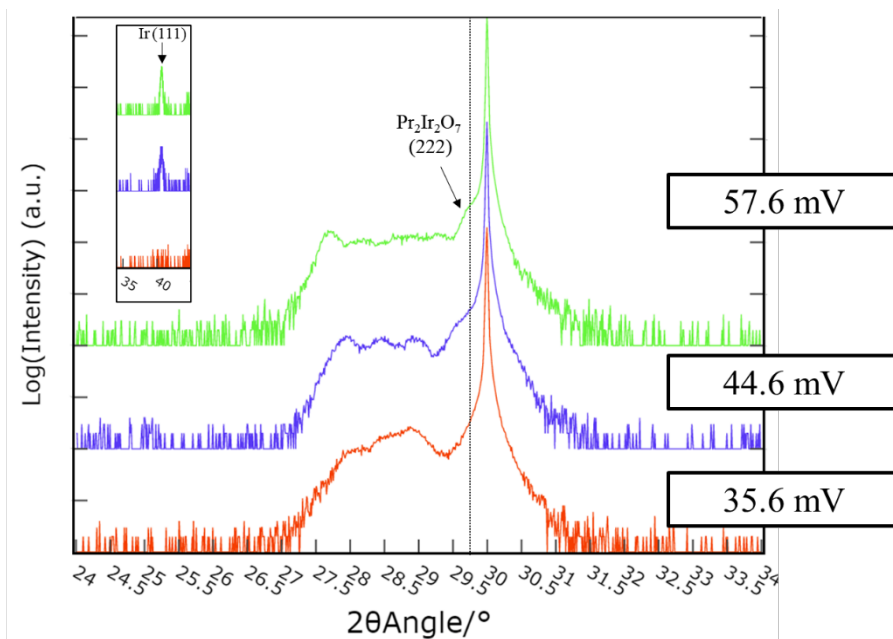


Figure 3.10 XRD scan of $\text{Pr}_2\text{Ir}_2\text{O}_7$ films grown with different laser fluence at substrate temperature of 1000°C and oxygen pressure $P_{O_2} = 0.05\text{mTorr}$. (Insert) position of iridium metal peak.

Depositions using the SPS mixed-oxide target supported the previous conclusion that low oxygen pressures and high laser fluence is necessary for the formation of the pyrochlore iridate phase and that the growth window, if it exists at all, is extremely narrow. Additionally, a variety of praseodymium oxide phases are observed in the XRD results, which may be a reason why the formation window for $\text{Pr}_2\text{Ir}_2\text{O}_7$ is so narrow.

3.2.3. Depositions with a Pr_6O_{11} target

Compared with other rare-earth oxides, praseodymium oxides can form a variety of phases. In addition to Pr_2O_3 and PrO_2 , there are at least five other suboxides that have been characterized in the literature. The general chemical formula of these suboxides is $\text{Pr}_n\text{O}_{2n-2}$,

where n can assume different values: 7, 9, 10, 11, 12⁷⁸. Additionally, different praseodymium oxides have diffraction peaks in a very narrow range, as shown in Figure 3.11⁷⁸, and strain induced by substrate would lead to a bias of peak positions. Therefore, matching the peaks of praseodymium oxides from PDF database is imprecise and often inconclusive.

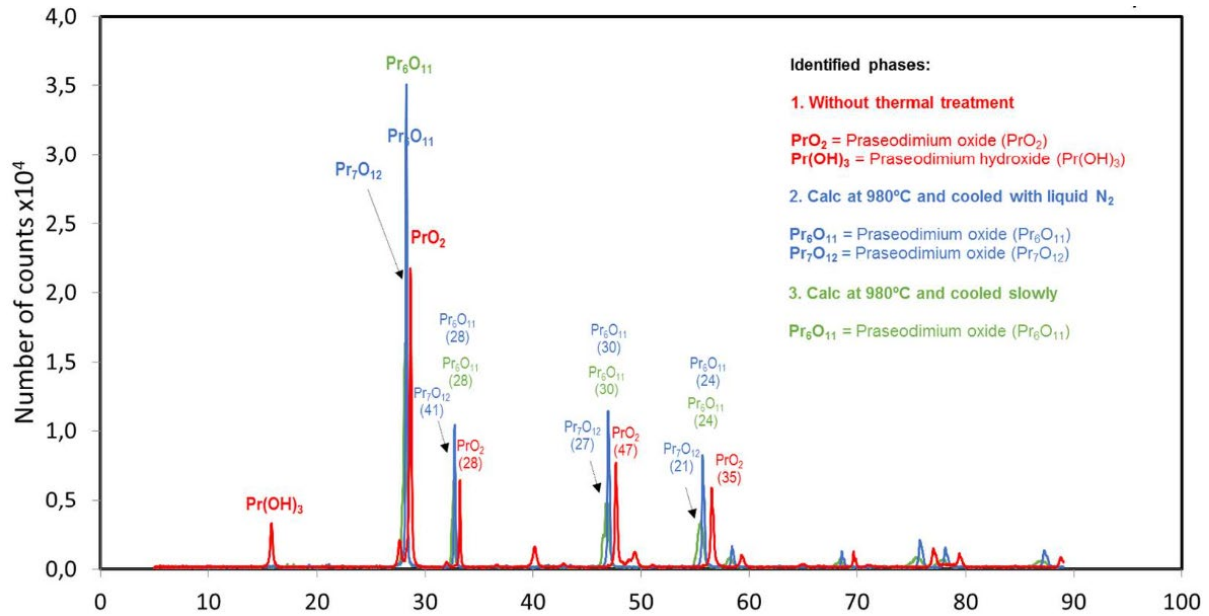


Figure 3.11 XRD peak positions of different praseodymium oxides

To investigate the change of praseodymium's valence in different conditions, a Pr_6O_{11} target was ordered from a commercial supplier. Several depositions were done at different oxygen pressures, using this target to grow films on YSZ(111) substrates at a fixed substrate temperature of 1000°C. The XRD results are shown in Figure 3.12. The peaks corresponding to different praseodymium valence states are marked as high, medium, and low. These peaks can be well matched to previous results, and behaviors are also similar. In the previous results, the iridate phase always appears together with several segregated praseodymium oxides that shows diffraction peaks around 27.9°, which is identified as the lowest valence of praseodymium in Figure 3.12. With the increase of oxygen pressure, this peak at 27.9° disappears, and other high valence phases are generated at 25.1°, 31.4° and 32.2°. In the growth of other iridates including pyrochlore $\text{Bi}_2\text{Ir}_2\text{O}_7$ ⁷⁹ and SrIrO_3 ⁸⁰, much higher oxygen pressure (~100 mTorr) are used, while in this experiment, iridate phase only shows in extremely low oxygen pressure environments. This can be explained by the high sensitivity of the valence of praseodymium.

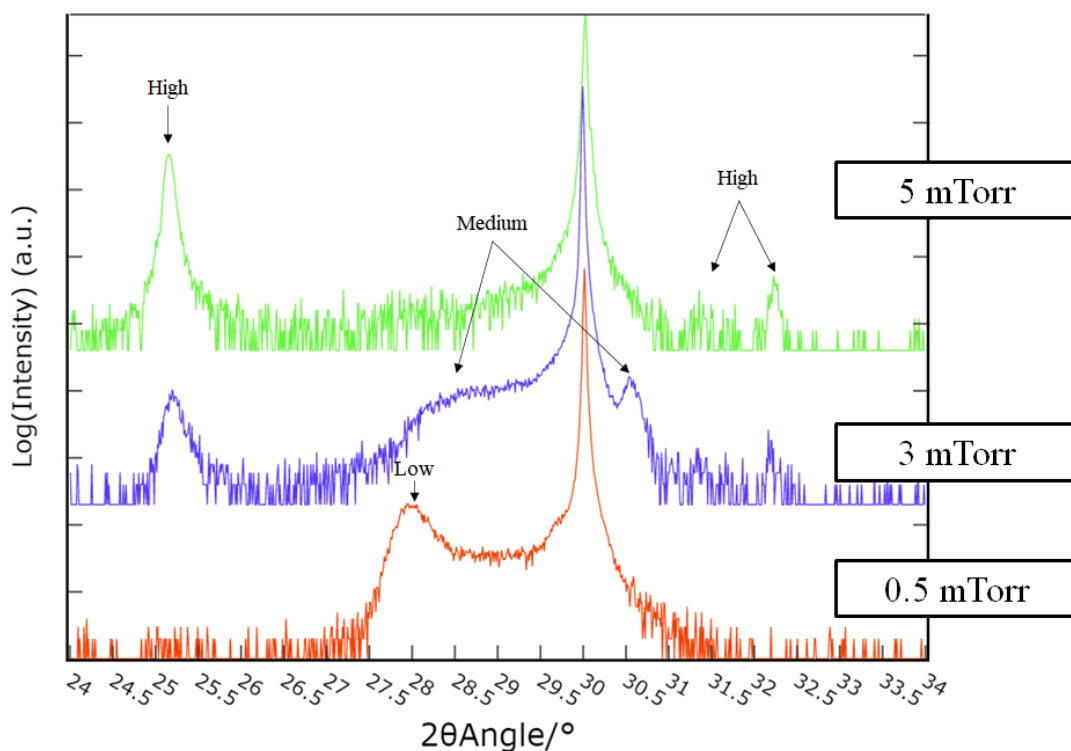


Figure 3.12 XRD narrow scan of praseodymium oxide films grown on YSZ substrate at substrate temperature of 1000°C at different oxygen pressure

3.2.4. Depositions in an inert gas

Laser ablation techniques are usually divided into two categories depending on the mean free path of the ionized species in the ablation plume. At low ambient pressures, when the mean free path of ions is larger than the distance between the ablation target and the substrate, the method is known as laser molecular beam epitaxy (LMBE). At high pressures, usually in the mTorr range, the mean free path becomes shorter than the target-film distance and the method is generally known as pulsed laser deposition (PLD). In the LMBE regime and at the lower end of the PLD regime, when film growth is done at low background pressures and at high laser fluence, the kinetic energy of the plasma plume may be high enough to result in a resputtering on the substrate surface.

Figure 3.13a⁸¹ illustrates the interaction between the plasma plume and the background gas when the background pressure is in the mTorr range. In this case, many collisions occur between the high-energy ions in the plasma and the ambient gas molecules, usually oxygen. A high-pressure shockwave front will form at the leading edge of the plume, compressing the plasma and making the plume significantly more luminous due to the collisions with oxygen. These gas-phase collisions transfer energy to the oxygen molecules and therefore reduce the kinetic energy of the ions in the plume that travel in the vertical direction towards the film surface, as shown in Figure 3.13b⁵⁸. Because the formation of the iridate phase requires a relatively low oxygen pressure of ~ 1 mTorr, reduction of the plume kinetic energy is possible by injecting a non-reactive gas into the film growth chamber. In this way, the total gas pressure and thus the plume shape and energy can be controlled independently of the oxygen partial pressure, which determines the oxidation kinetics of the film.

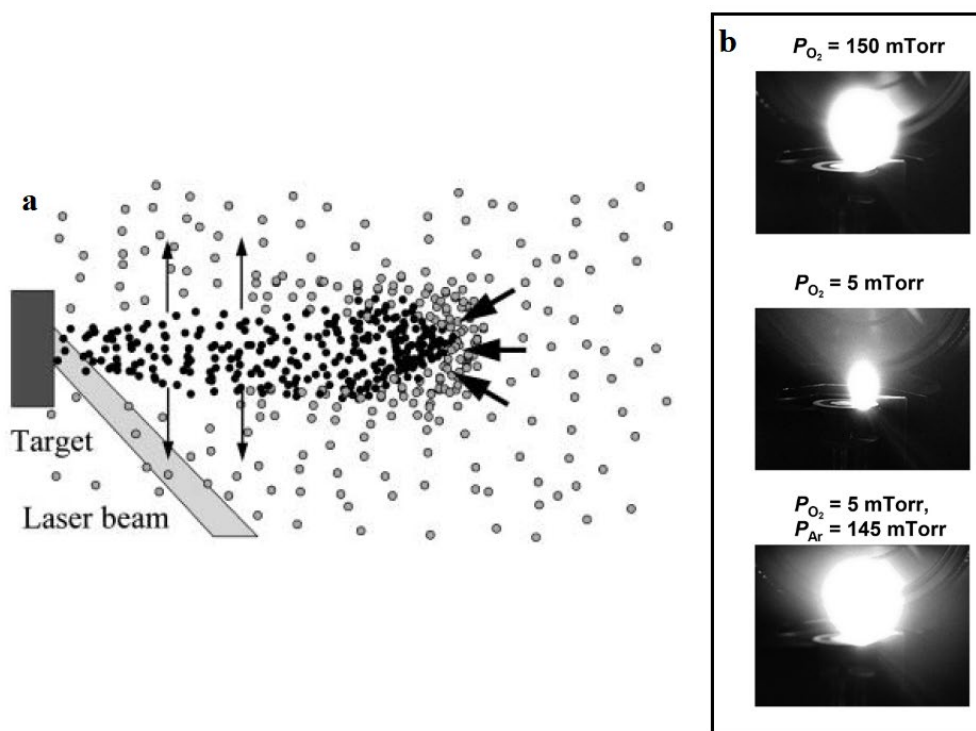


Figure 3.13 (a) schematic for the interaction between plume (black circles) and background gas (grey circles). (b) Plasma plume generated at different conditions.

The use of several inert gases in the iridate PLD growth was studied by introducing a gas mixing setup, as shown in Figure 3.14. Oxygen and an inert gas can be mixed in the mixing cylinder at a desired ratio. Then mixed gas was fed into the chamber through a molecular leak valve to control the chamber pressure, as usual. After deposition, the gas mixture was evacuated through a bypass line connected to the loading chamber.

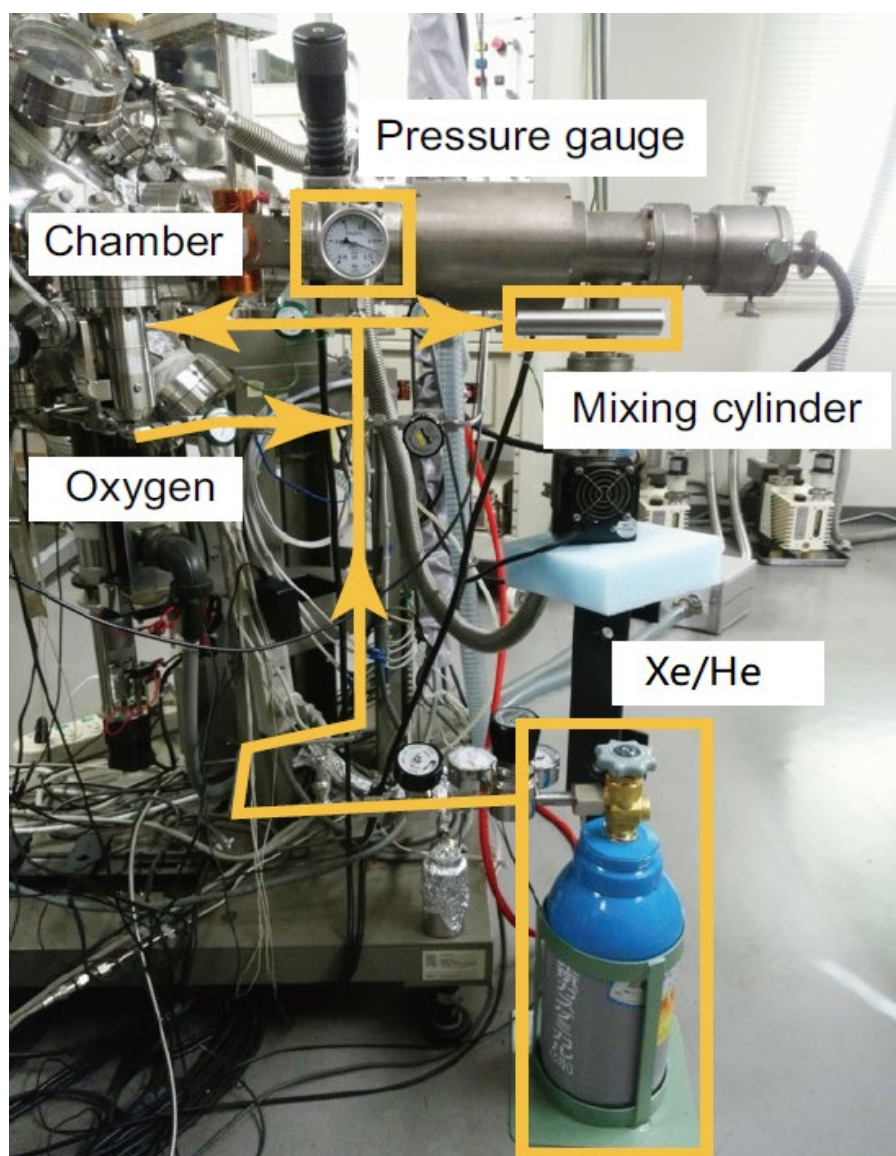


Figure 3.14 Photograph of the setup for mixing inert gas with oxygen.

Xenon was first utilized to increase the background pressure. Xe was selected because the atomic mass of Xe (131.3) is close to Ir (192.2), suggesting that efficient energy transfer from Ir to Xe would occur even if only a few gas collisions take place. Several films were fabricated at a fixed oxygen partial pressure of $P_{O_2} = 0.1$ mTorr and a substrate temperature of 1000°C with different Xe mixing ratios from 10% to 90%. XRD scans of these film are shown in Figure

3.15. Narrow scans show quite similar behavior, regardless of the Xe/O₂ mixing ratio. Although praseodymium oxide peaks appeared in the typical low-valence positions, no iridate peak was found in these films. However, with the increasing Xe/O₂ ratio, the iridium metal peak gradually disappeared (Figure 3.15 insert), which indicates that usage of Xe can reduce the formation of iridium metal without affecting the valence of praseodymium. Moreover, surface characterization by AFM, as shown in Figure 3.16, indicated that the surface roughness can be strongly reduced by the increase of the Xe/O₂ ratio.

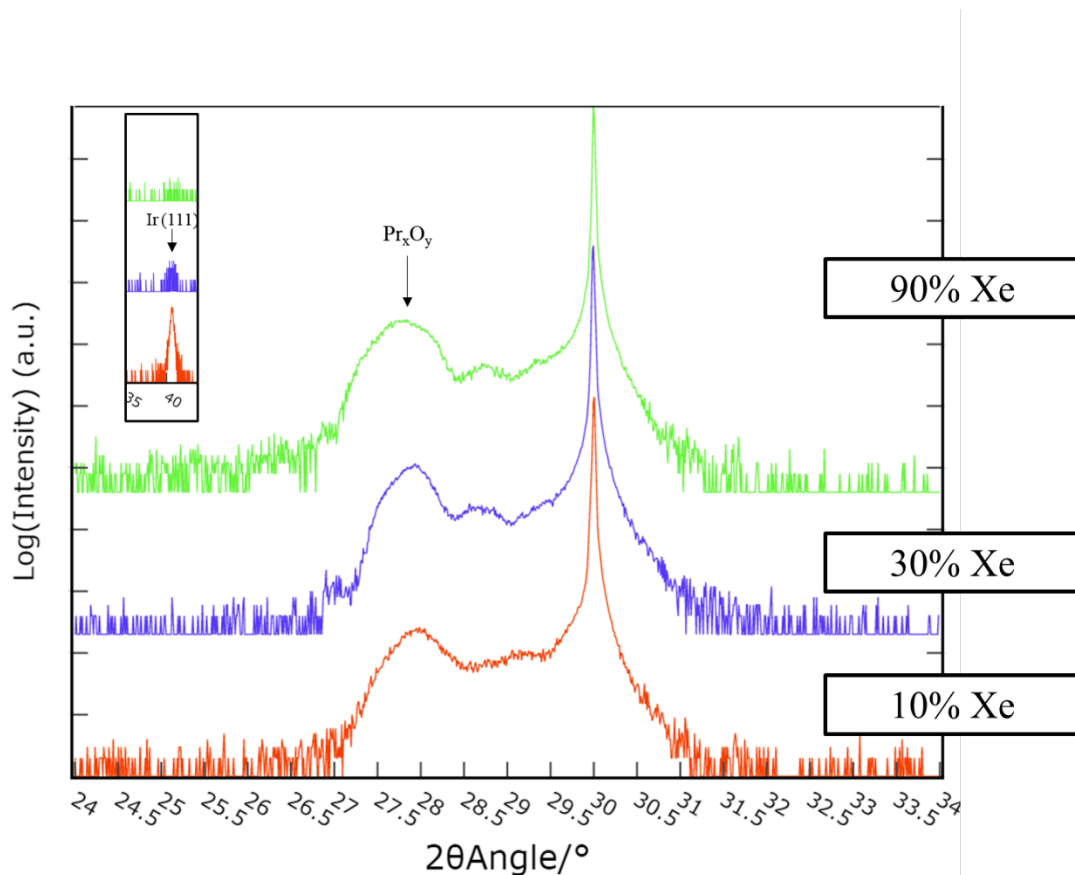


Figure 3.15 XRD scan of Pr₂Ir₂O₇ films grown with different Xe mixing ratio. Substrate temperature is 1000°C, oxygen pressure PO₂ is 0.05mTorr. (Insert) position of iridium metal peak.

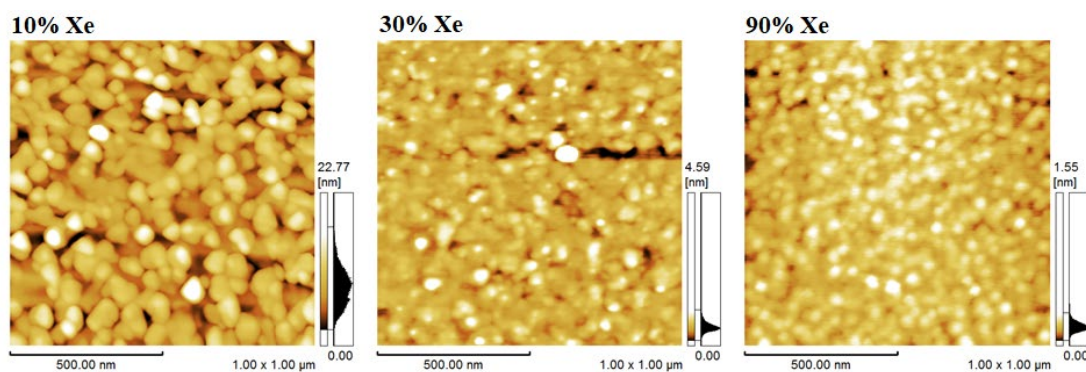


Figure 3.16 AFM image of films grown with different Xe mixing ratios.

Because the atomic mass of xenon is relatively heavy (131.3) and is close to iridium (192.2) and praseodymium (140.9), any gas-phase collisions would result in a large momentum change, deflecting the heavy iridium or praseodymium atoms out of the plume. Adding a heavy inert gas to the process thus leads to an inadvertent stoichiometry shift of the plume and is ultimately not advantageous.

The collisions pattern is quite different when a very light noble gas such as Helium is used. Figure 3.17 shows an illustration of the 2 different collision pattern. After colliding with a heavy atom, heavy ions in the plasma plume are deflected out of the plume. While this reduces the average kinetic energy of the plume, it also sharply reduces the deposition rate, even at relatively low total background gas pressures. In contrast, each collision event with a light gas would only slightly reduce the kinetic energy of a heavy atom in the plume, but the deflection of the heavy atom would also be small. If a much higher total pressure is used, each atom in the plume may undergo many collisions with the inert gas atoms but the average deflection from the original flight path would be close to zero. This means that a light inert gas is more suitable for plume kinetic energy control without incurring a stoichiometry shift of the atomic species arriving at the film surface.

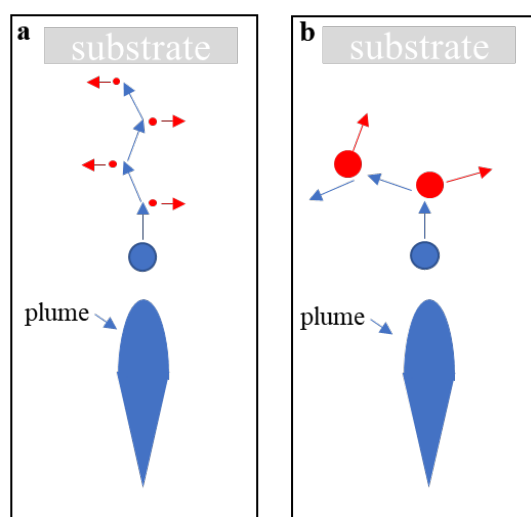


Figure 3.17 (a) Collision pattern in light inert gas atmosphere.
(b) collision pattern in heavy inert gas atmosphere. (blue circle)
ion from plasma plume. (red circle) inert gas atom.

Therefore, Helium was used for further study of the influence of an inert buffer gas on iridate film growth. Since the previous results obtained with the Xe buffer indicated that a high buffer gas ratio has a more obvious effect, the He concentration was kept in 97%. Depositions were done at different oxygen partial pressures from 0.015 mTorr to 1.5 mTorr and a substrate temperature of 1000°C.

Figure 3.18 shows the XRD results for these films. The iridate phase can be only obtained in a film grown at 0.015 mTorr oxygen pressure. In contrast to the results from Xe experiments, all films show the iridium metal phase, while the praseodymium's valence is highly varied. Since the oxygen pressure must be kept at a low level, the total pressure is still low even with a He/O₂ ratio of 97%. Therefore, a higher ratio of 99.5% was utilized, while oxygen partial pressure was 0.5 mTorr, with a total pressure of 100 mTorr. At this pressure, only a single crystalline peak was obtained in the XRD scan, as shown in Figure 3.19. This phase was identified as Pr₃IrO₇(110) based on the available data in the PDF database and no iridium metal nor praseodymium oxide was found in this film.

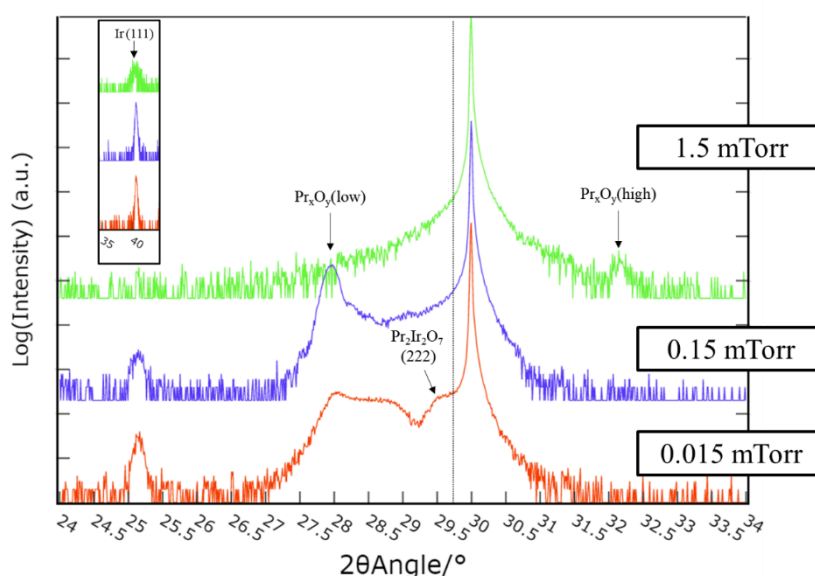


Figure 3.18 XRD scan of Pr₂Ir₂O₇ films grown at different oxygen partial pressures with 97% He. Substrate temperature is 1000°C. (Insert) position of iridium metal peak.

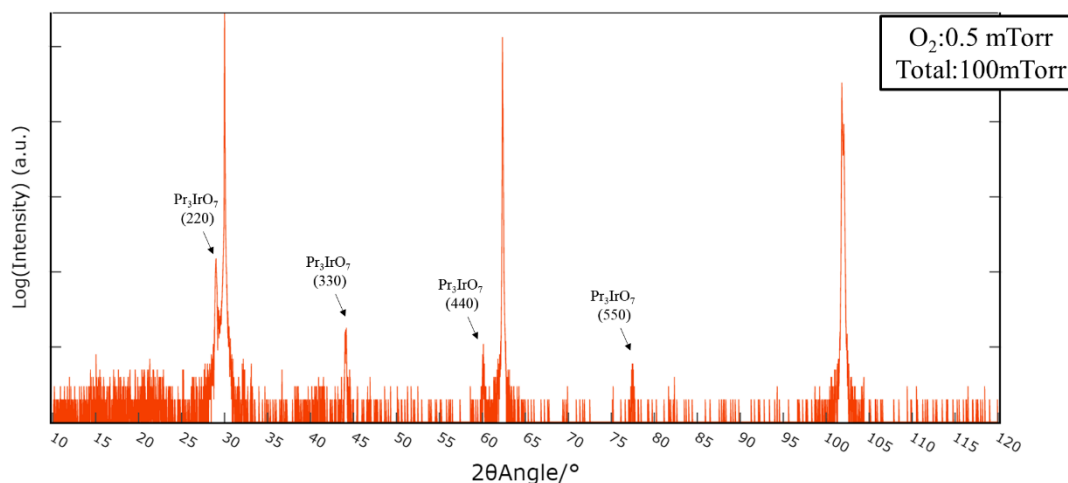


Figure 3.20 XRD wide-area scan of film made at 0.5 mTorr oxygen partial pressure and 100 mTorr total pressure. Substrate temperature is 1000°C.

Pr_3IrO_7 crystallizes in an orthorhombic superstructure of a cubic fluorite with a space group Cmcm , as shown in Figure 3.20⁸². It often appears as an impurity composition in the synthesis of $\text{Pr}_2\text{Ir}_2\text{O}_7$ ⁸³. The formation of Pr_3IrO_7 probably happens because of the perturbation of the praseodymium valence by the presence of helium. However, it has been demonstrated that helium can also reduce the formation of iridium metal but requires a much higher total process pressure.

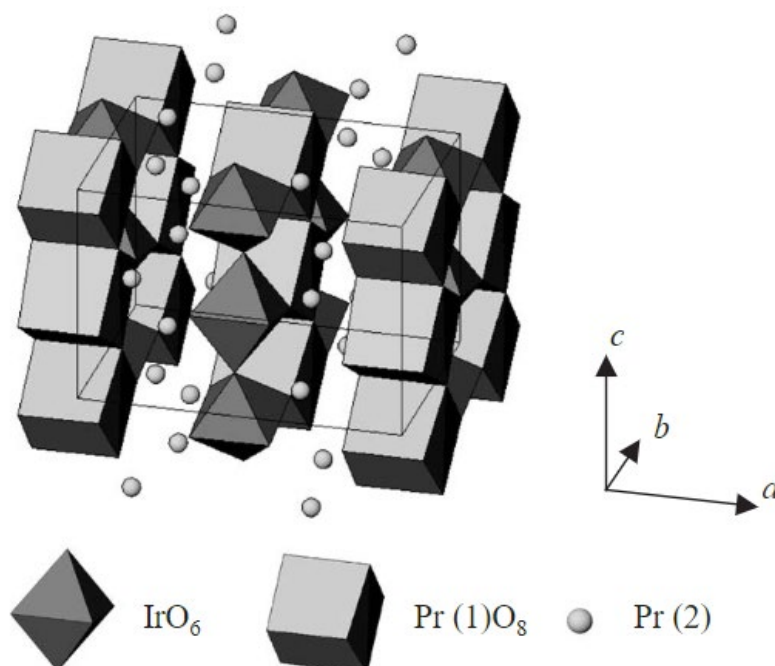


Figure 3.19 Crystal structure of Pr_3IrO_7 .

3.3 Growth of $\text{La}_2\text{Ir}_2\text{O}_7$

Since lanthanum has the largest ionic radius among the lanthanides, replacing Pr with La in the pyrochlore iridate would correspondingly increase the lattice parameter. The pyrochlore lattice parameter is known to affect the metal-insulator transition behavior and may lead to more obvious nontrivial electronic properties than the praseodymium pyrochlore. Compared to the abundant phases of praseodymium oxides, there is usually only one stable valence state for the lanthanum ion, La^{3+} . Although the pyrochlore lanthanum iridate is not known to form a bulk single crystal due to the large A-site ionic radius, it is still possible to grow a meta-stable pyrochlore phase within a quas-2D layer of a thin film.

A target for $\text{La}_2\text{Ir}_2\text{O}_7$ film growth was prepared by SPS in a similar way to the mixed-oxide target used for the $\text{Pr}_2\text{Ir}_2\text{O}_7$ film studies. The La_2O_3 and IrO_2 powders were mixed with a Ir:La ratio of 3:1 to compensate for the loss of iridium. To verify the stability of the valence of lanthanum, initial depositions were done at 900°C at different oxygen pressures without the addition of an inert gas, as shown in Figure 3.21. The predicted bulk position of $\text{La}_2\text{Ir}_2\text{O}_7$ is marked with a dashed line. These films show high similarity, even though the oxygen pressure changed by a factor of 20. The diffraction peak that appears at 24.8° is identified as La_2O_3 . Additionally, a broad intensity increase is seen over a wide range of diffraction angles between the La_2O_3 and substrate peaks. The diffraction intensity in this region seems to consist of numerous small and broad. For getting a more explicit understanding, additional depositions were done at a higher temperature of 1000°C . Figure 3.22 shows the XRD scans of the films. The La_2O_3 peak still appears in both films. However, the middle part between the La_2O_3 and substrate peaks differs significantly. In the 3 mTorr film, the peak is identified as $\text{La}_3\text{IrO}_7(220)$, which is similar to the previous praseodymium experiment. When oxygen pressure was increased to 10 mTorr, a new peak appeared near the substrate peak, which may be a $\text{La}_3\text{Ir}_3\text{O}_{11}(3\ 1\ 0)$ peak, although the lattice matching would be unexpected for the YSZ(111) substrate surface. $\text{La}_3\text{Ir}_3\text{O}_{11}$ has been reported to have an unusual +4.33 valence state of iridium⁸⁴, which would correspond to the disappearance of the iridium metal peak (Figure 3.22 insert). Nonetheless, no pyrochlore phase was obtained in these films.

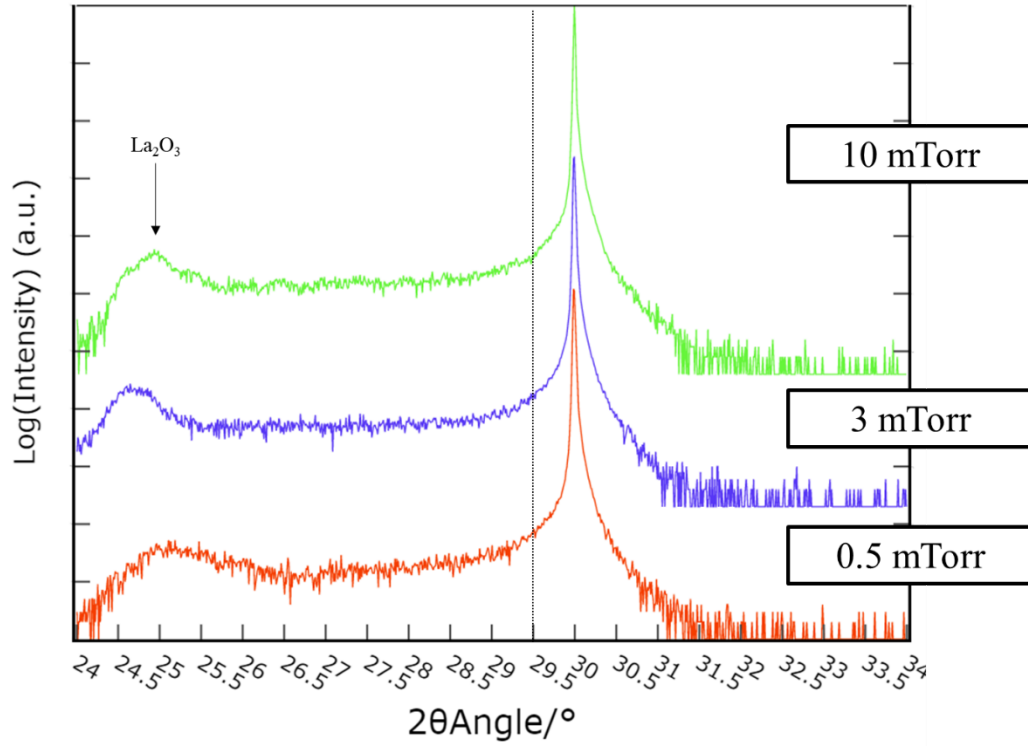


Figure 3.21 XRD scans of La-Ir-O films grown at different oxygen pressures and a substrate temperature of 900°C. The dashed line marks the estimated pyrochlore position.

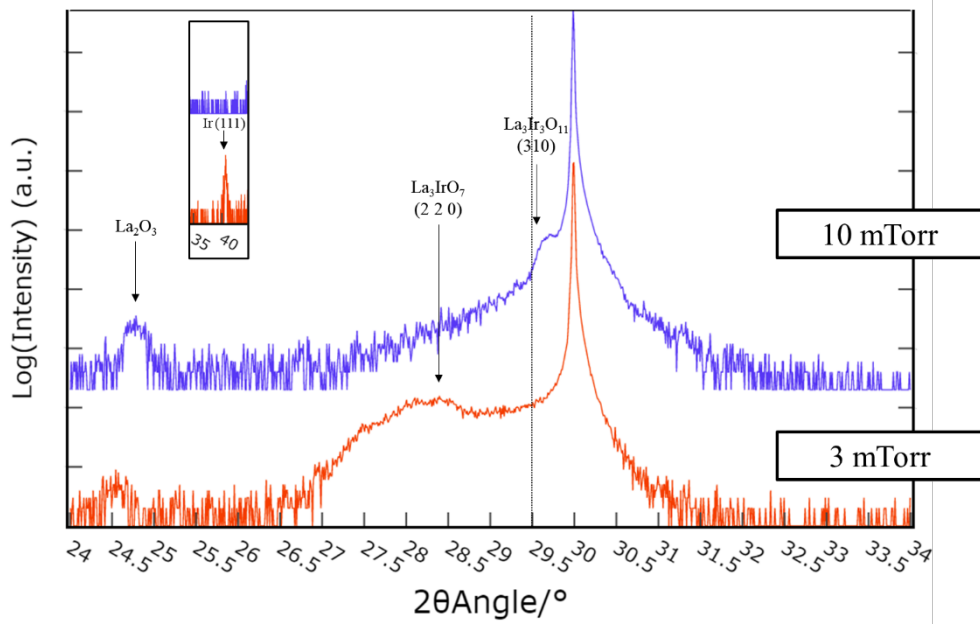


Figure 3.22 XRD scan of films grown at different oxygen pressure at substrate temperature of 1000°C. Dash line denotes the estimated pyrochlore position. (Insert) position of iridium metal peak.

Compared to praseodymium, the valence of lanthanum was demonstrated to be stable, although several polymorphs of La oxides may appear, complicating the XRD analysis. A more serious complication, however, is the existence of competing phases of lanthanum iridates, which may lead to an equally narrow growth window for $\text{La}_2\text{Ir}_2\text{O}_7$ as was observed for $\text{Pr}_2\text{Ir}_2\text{O}_7$, albeit for a different reason. Further depositions with more accurate process control would be necessary if a growth window exists at all.

Chapter 4. Influence of iridium clustering

It's well known that iridium oxides are highly volatile and that iridium metal is prone to oxidize to a gaseous IrO_3 phase, especially in the temperature range that is most suitable for pyrochlore synthesis. This is usually considered to be the main obstacle to growing iridate thin films. However, in the experiments of growing pyrochlore iridates, an obvious phase separation phenomenon between praseodymium oxides and iridium metal was observed in many films, including those films that do show the presence of reacted iridate phases. This phenomenon is not unique to this work, but has been reported in other works of pyrochlore iridate growth as well^{63,79}. In a simplified film growth model, iridium atoms would be expected to react with rare-earth atoms and oxygen while migrating on the film surface. However, phase separation indicates that iridium atoms rapidly form macroscopic clusters before or without oxidizing and reacting with the rare-earth atoms.

Since cluster formation is a kinetic process, related to the rate of surface migration of adatoms on a film surface, the clustering issue was studied by making several depositions at different laser frequencies from 0.5 to 10 Hz using the mixed-oxide La-Ir target. The relaxation times between the deposition pulses thus varied from 0.1 to 2 seconds. Iridium metal clusters may form during this period if the metal migration rate is high and the oxidation process is slow. It may be reasonable to expect that a longer waiting time between the laser pulses would lead to the growth of larger metal clusters that would show a stronger and sharper Ir(111) diffraction peak in the XRD scans.

Figure 4.1 shows the XRD results. In contrast to the initial expectations, the phase separation was even stronger in films grown at higher laser repetition rates, which means that the migration rate of iridium on the substrate surface could be much higher than originally considered and that metal clustering happens on time scales that are much shorter than 100 ms, which is the shortest available pulse interval for the excimer laser. Theoretical results⁸⁵ show that the Ir(111) surface has the lowest surface energy, especially for the first layer, compared to other surface indices. Formation of iridium metal clusters with the [111] orientation is thus the expected behavior. Moreover, there are very few published reports of in-situ growth of iridate thin film with the [111] orientation. Most perovskite-related iridate phases, for examples are grown on (001) substrate surfaces. It has been demonstrated that iridium is more inclined to cluster rather than react with rare-earth atoms, which may be the actual major obstacle to growing iridate thin films on (111) substrates.

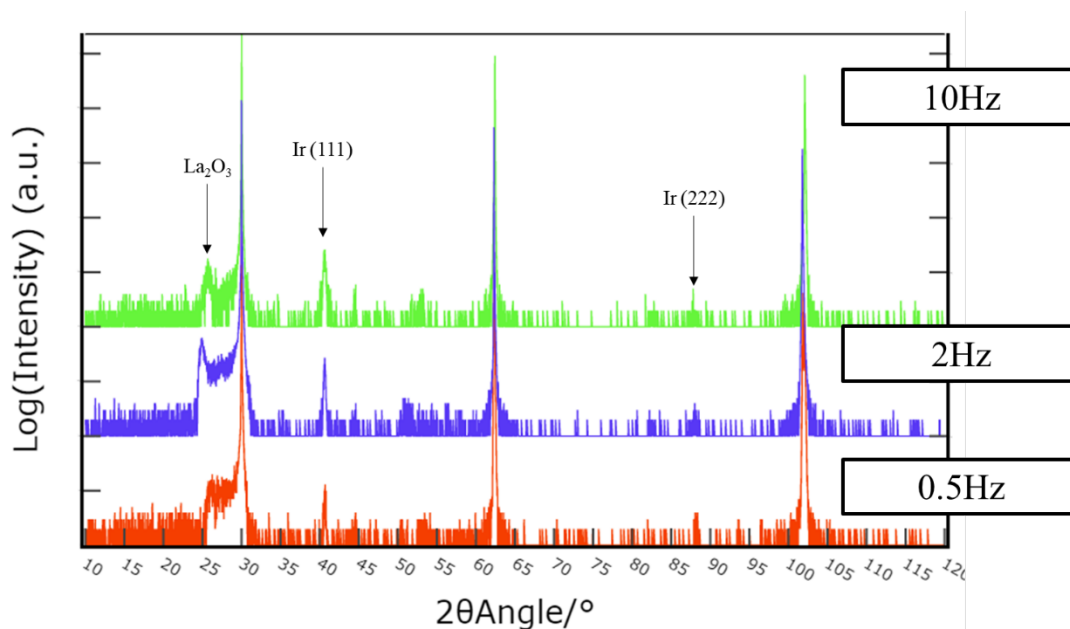


Figure 4.1 XRD wide-area scan of films made with laser frequency from 0.5Hz to 10Hz using La-Ir target. Substrate temperature is 1000°C; oxygen pressure is 10mTorr.

Figure 4.2 shows the phase formation diagram for iridium oxides and iridium metal⁸⁶, where the shaded part is the region where the iridium metal phase appeared in this work. This behavior is unusual since higher temperatures should be a more suitable for the formation of iridium metal phase according to the Ellingham diagram. However, in practice, iridium metal disappears at high temperatures at same oxygen pressure. This can be ascribed to the formation of IrO₃, which is commonly thought to happen in the nonequilibrium surface region when the ablation plasma plume hits the film surface.

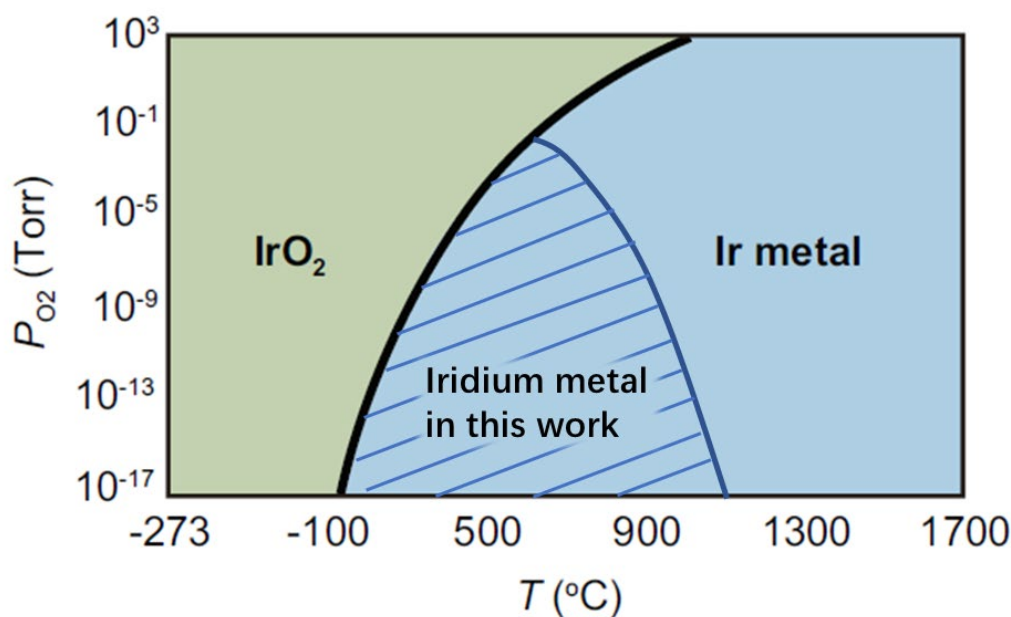


Figure 4.2 Phase formation diagram of iridium metal and iridium oxide. Shaded part denotes the region where iridium metal phase was observed in this work.

Nonetheless, this behavior strongly suggests that the oxidation and sublimation processes may happen regardless of the presence of oxygen or lanthanide ions in the plume. To verify the role of Ir evaporation, a pure iridium metal sheet was used as a target to deposit thin metal films directly on YSZ substrates. Depositions were done at 10 mTorr oxygen pressure and substrate temperature of 1000°C with different laser pulse rates. Figure 4.3 shows the XRD results. At lower laser pulse rates, i.e., longer relaxation periods between ablation pulses, the intensity of the iridium metal peak became obviously smaller, which demonstrates that the clusters do not grow in size with the increase of the pulse interval, as would be expected for a slow surface migration mechanism. Instead, the clusters form rapidly, on millisecond time scales, and then gradually diminish in size as the oxidation of iridium and IrO₃ sublimation occurs on the substrate surface on a time scale of seconds.

Additionally, another film was deposited using interval deposition. The oxygen pressure was reduced to 1 mTorr (10 times lower than the previous experiments) and the laser pulse rate was set at 5 Hz. After every 200 laser pulses, the film surface was allowed to relax for 30 seconds. As shown in Figure 4.4, Compared to the film made by continuous deposition, this interval-deposited film showed a much lower intensity of the iridium metal peaks even though the rapid deposition sequences at 5 Hz should be more favorable for the formation of large iridium metal clusters. This result shows that there is strong evaporation loss even for large Ir clusters, although if the clusters are rapidly grown to a certain size, the stability against oxidation may improve. This of course, is not helpful from the point of view of synthesizing a fully reacted iridate pyrochlore.

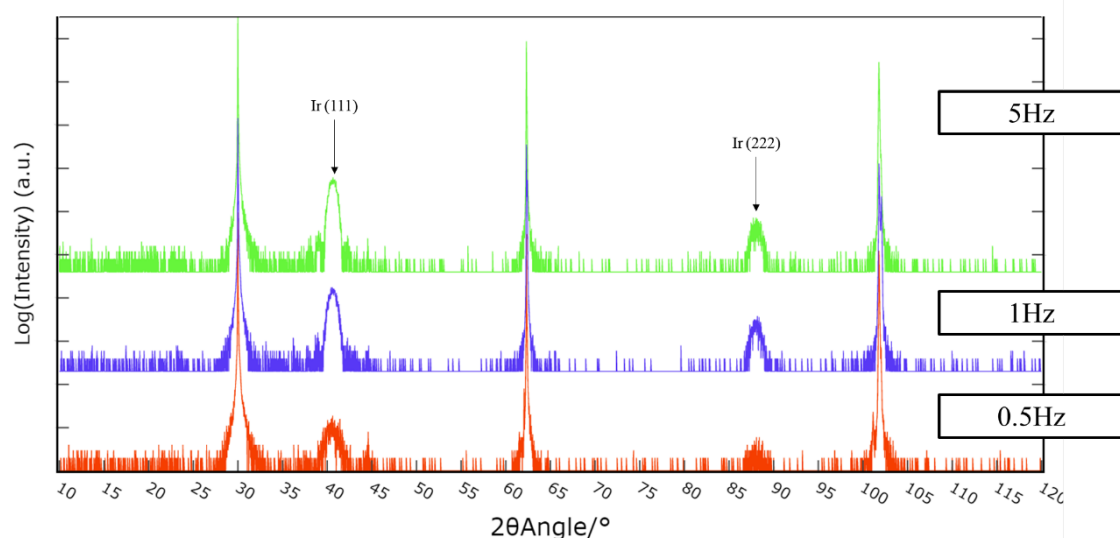


Figure 4.3 XRD wide-area scans of films grown at laser pulse rates of 0.5Hz to 5Hz using an Ir metal target. Substrate temperature was 1000°C and the oxygen pressure was 10mTorr.

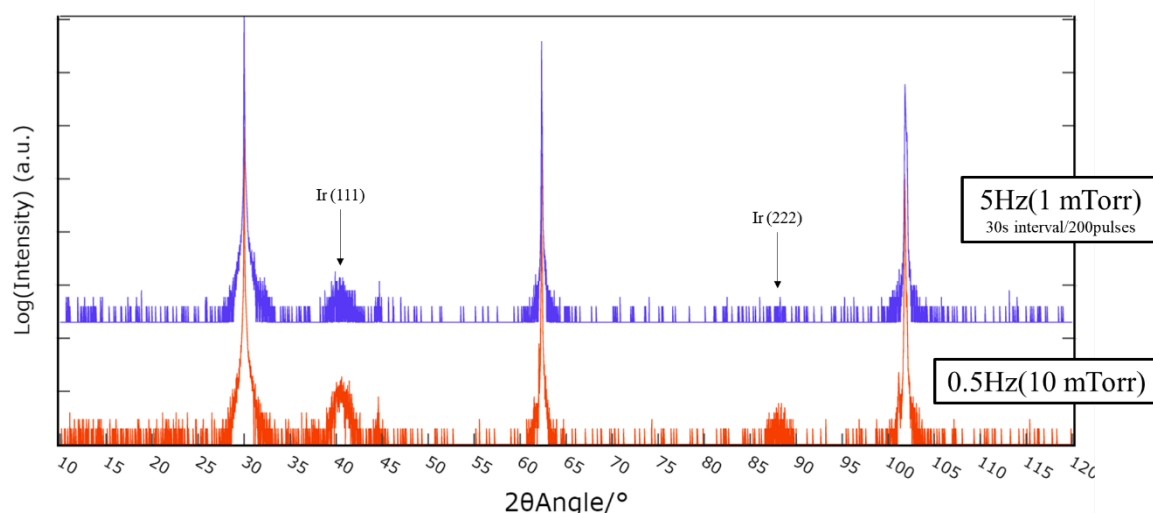


Figure 4.4 XRD wide-area scan of Ir metal films grown by continuous deposition and interval deposition.

A recent computational result⁸⁷ has suggested that iridium metal with a (111) surface has the highest probability to be oxidized, while other surface facets would be expected to be moderately stable. The temperature and oxygen pressure can separately affect the different steps of the oxidation process. The facet-selective oxidation mechanism of Ir metal can reasonably explain the phenomenon observed in the depositions of pure iridium metal in an oxygen environment. The iridium metal was under a continuous oxidation process during the deposition and became more stable only when surface facets other than (111) appeared. This etching-like process requires a certain volume and causes the iridium metal always to form arrowhead shapes on a substrate surface. Although it's easy to form iridium metal clusters on a (111) surface, the high volatility provides an opportunity to remove the metal phase.

Chapter 5. Summary

In this work, we attempted the growth of $R_2Ir_2O_7$ ($R = La, Pr$) thin films on YSZ(111) substrate by PLD using different targets and analyzed the influence induced by ambient conditions as well as some intrinsic properties of materials.

A remarkably narrow growth window with high temperature and low oxygen pressure was confirmed by depositions using a solid-state reaction $Pr_2Ir_2O_7$ target, while this extreme condition may also lead to a defect-fluorite phase. Moreover, iridium metal can be also observed from XRD $\theta/2\theta$ scan, which hinders from measuring the transportation properties. However, surface of films fabricated with this target was strongly contaminated by particles from target, which is caused by the target's lack of hardness.

For improving the hardness, an iridium-rich target was made by SPS using a ground powder of mixed Pr_2O_3 and IrO_2 . Depositions using this target confirmed again the narrow window. Fluence-dependent could be investigated using this target, which showed a fluence threshold of both generation of iridium and formation of iridate.

Since numerous praseodymium oxide phases showed in previous experiments, the valence of praseodymium was considered to be a potential key factor of the growth of praseodymium iridate. This conjecture was then confirmed by depositions using a Pr_6O_{11} target. Valence of praseodymium shows a high sensitivity to the oxygen pressure, even in low pressure, whereas the praseodymium in $Pr_2Ir_2O_7$ requires the lowest valence, which could be the reason for the narrow oxygen pressure window.

Inert gas was used to reduce the kinetic energy of plasma plume. Xe and He gas were utilized in this experiment. They showed different behaviors due to the considerable difference of atomic mass. Inert gas was demonstrated to be able to reduce the formation of iridium metal, although a high pressure is required for light gas.

In that lanthanum has a bigger ionic radius and more stable valence state, we also made attempts to grow $La_2Ir_2O_7$ thin film. The stability of valence of lanthanum was demonstrated by several depositions; however, due to the various competing lanthanum iridate phases, no pyrochlore was obtained.

Phase separation was considered as a major obstacle of growing pyrochlore iridates. Depositions using La-Ir target and pure iridium metal target demonstrated the extremely high migration rate of iridium on substrate surface. Further experiments revealed the oxidation of iridium also happens on substrate and is related to the volume of iridium metal. Direction of surface is the key factor related to this behavior; thus, this conclusion can be applied to other iridates thin film grown with [111] orientation.

Acknowledgements

Upon the completion of this thesis, I am grateful to those who have offered me encouragement and support during my two year's study.

First and foremost, the profound gratitude is given to my respectable supervisors Mikk Lippmaa who gave me the opportunity to work in this lab and instructed me in finishing my master's work. I have learnt a lot from him in these 2 years, which is the most precious experience in my life.

Secondly, as my tutor, Dr. Jiyeon Lee gave me many helps in both life and study. Mr. Shuji Ezura also helped me a lot for my life in Japan. I would like to give them my sincere thanks.

I would also like to thank Ms. Junko Nagayama for helping me handle administrative works, and thank Dr. Taizo Mori, Ms. Hanako Kuramochi that I could spend wonderful days because of them.

Besides, I want to thank my friends who gave my many suggestions and helps. And I want to thank my family who always support me.

Xianming Yu

References

1. Erwin, S. C. When is a metal not a metal? *Nature* **441**, 295–196 (2006).
2. De Boer, J. H. & Verwey, E. J. W. Semi-conductors with partially and with completely filled 3d-lattice bands. *Proc. Phys. Soc.* **49**, 59–71 (1937).
3. Imada, M., Fujimori, A. & Tokura, Y. Metal-insulator transitions. *Rev. Mod. Phys.* (1998) doi:10.1103/revmodphys.70.1039.
4. Kohsaka, Y. *et al.* How Cooper pairs vanish approaching the Mott insulator in Bi₂Sr₂CaCu₂O₈+ δ . *Nature* (2008) doi:10.1038/nature07243.
5. Hubbard, J. Electron correlations in narrow energy bands. *Proc. R. Soc. London. Ser. A. Math. Phys. Sci.* (1963) doi:10.1098/rspa.1963.0204.
6. Zhang, F. C. & Rice, T. M. Effective Hamiltonian for the superconducting Cu oxides. *Phys. Rev. B* **37**, 3759–3761 (1988).
7. Griffin, S. M., Staar, P., Schulthess, T. C., Troyer, M. & Spaldin, N. A. A bespoke single-band Hubbard model material. *Phys. Rev. B* **93**, 075115 (2016).
8. Mandrus, D. *et al.* Continuous metal-insulator transition in the pyrochlore Cd₂Os₂O₇. *Phys. Rev. B - Condens. Matter Mater. Phys.* (2001) doi:10.1103/PhysRevB.63.195104.
9. Kim, B. J. *et al.* Novel $j_{\text{eff}}=1/2$ mott state induced by relativistic spin-orbit coupling in Sr₂IrO₄. *Phys. Rev. Lett.* **101**, 076402 (2008).
10. Cowan, R. D. & of California Press, U. *The Theory of Atomic Structure and Spectra.* (University of California Press, 1981).
11. Shanavas, K. V., Popović, Z. S. & Satpathy, S. Theoretical model for Rashba spin-orbit interaction in d electrons. *Phys. Rev. B - Condens. Matter Mater. Phys.* **90**, 165108 (2014).
12. Jackeli, G. & Khaliullin, G. Mott insulators in the strong spin-orbit coupling Limit: From Heisenberg to a Quantum Compass and Kitaev Models. *Phys. Rev. Lett.* (2009) doi:10.1103/PhysRevLett.102.017205.
13. Witczak-Krempa, W., Chen, G., Kim, Y. B. & Balents, L. Correlated quantum phenomena in the strong spin-orbit regime. *Annu. Rev. Condens. Matter Phys.* (2014) doi:10.1146/annurev-conmatphys-020911-125138.
14. Klitzing, K. V., Dorda, G. & Pepper, M. New method for high-accuracy determination of the fine-structure constant based on quantized hall resistance. *Phys. Rev. Lett.* **45**, 494–497 (1980).
15. Day, C. Quantum spin hall effect shows up in a quantum well insulator, just as predicted. *Phys. Today* **61**, 19–23 (2008).

16. Kane, C. L. & Mele, E. J. Quantum Spin hall effect in graphene. *Phys. Rev. Lett.* **95**, 226801 (2005).
17. Gao, H., Venderbos, J. W. F., Kim, Y. & Rappe, A. M. Topological Semimetals from First Principles. *Annu. Rev. Mater. Res.* **49**, 153–183 (2019).
18. Özdemir, Ş. K. Fermi arcs connect topological degeneracies. *Science* vol. 359 995–996 (2018).
19. Fang, Z. *et al.* The anomalous Hall effect and magnetic monopoles in momentum space. *Science* (80-.). **302**, 92–95 (2003).
20. Huang, X. *et al.* Observation of the chiral-anomaly-induced negative magnetoresistance: In 3D Weyl semimetal TaAs. *Phys. Rev. X* (2015) doi:10.1103/PhysRevX.5.031023.
21. Potter, A. C., Kimchi, I. & Vishwanath, A. Quantum oscillations from surface Fermi arcs in Weyl and Dirac semimetals. *Nat. Commun.* **5**, 1–6 (2014).
22. Lv, B. Q. *et al.* Experimental discovery of weyl semimetal TaAs. *Phys. Rev. X* (2015) doi:10.1103/PhysRevX.5.031013.
23. Xu, S. Y. *et al.* Discovery of a Weyl fermion semimetal and topological Fermi arcs. *Science* (80-.). **349**, 613–617 (2015).
24. Wan, X., Turner, A. M., Vishwanath, A. & Savrasov, S. Y. Topological semimetal and Fermi-arc surface states in the electronic structure of pyrochlore iridates. *Phys. Rev. B - Condens. Matter Mater. Phys.* (2011) doi:10.1103/PhysRevB.83.205101.
25. Wang, Q. *et al.* Large intrinsic anomalous Hall effect in half-metallic ferromagnet Co₃Sn₂S₂ with magnetic Weyl fermions. *Nat. Commun.* (2018) doi:10.1038/s41467-018-06088-2.
26. Yoshimura, Y., Onishi, W., Kobayashi, K., Ohtsuki, T. & Imura, K. I. Comparative study of Weyl semimetal and topological/Chern insulators: Thin-film point of view. *Phys. Rev. B* (2016) doi:10.1103/PhysRevB.94.235414.
27. Anderson, P. W. Resonating valence bonds: A new kind of insulator? *Mater. Res. Bull.* (1973) doi:10.1016/0025-5408(73)90167-0.
28. Bernu, B., Lecheminant, P., Lhuillier, C. & Pierre, L. Exact spectra, spin susceptibilities, and order parameter of the quantum Heisenberg antiferromagnet on the triangular lattice. *Phys. Rev. B* (1994) doi:10.1103/PhysRevB.50.10048.
29. Iaconis, J., Liu, C., Halász, G. B. & Balents, L. Spin liquid versus spin orbit coupling on the triangular lattice. *arXiv* (2017) doi:10.21468/scipostphys.4.1.003.
30. Kitaev, A. Anyons in an exactly solved model and beyond. *Ann. Phys. (N. Y.)*. (2006) doi:10.1016/j.aop.2005.10.005.
31. Li, Y. *et al.* Gapless quantum spin liquid ground state in the two-dimensional spin-1/2 triangular antiferromagnet YbMgGaO₄. *Sci. Rep.* (2015) doi:10.1038/srep16419.

-
32. Li, Y. *et al.* Rare-Earth Triangular Lattice Spin Liquid: A Single-Crystal Study of YbMgGaO₄. *Phys. Rev. Lett.* (2015) doi:10.1103/PhysRevLett.115.167203.
 33. Shen, Y. *et al.* Evidence for a spinon Fermi surface in a triangular-lattice quantum-spin-liquid candidate. *Nature* (2016) doi:10.1038/nature20614.
 34. Lv, B., Qian, T. & Ding, H. Angle-resolved photoemission spectroscopy and its application to topological materials. *Nature Reviews Physics* (2019) doi:10.1038/s42254-019-0088-5.
 35. Shinaoka, H., Motome, Y., Miyake, T., Ishibashi, S. & Werner, P. First-principles studies of spin-orbital physics in pyrochlore oxides. *Journal of Physics Condensed Matter* (2019) doi:10.1088/1361-648X/ab162f.
 36. Subramanian, M. A. & Sleight, A. W. Chapter 107 Rare earth pyrochlores. *Handbook on the Physics and Chemistry of Rare Earths* vol. 16 225–248 (1993).
 37. Schaffer, R., Kin-Ho Lee, E., Yang, B. J. & Kim, Y. B. Recent progress on correlated electron systems with strong spin-orbit coupling. *Reports on Progress in Physics* (2016) doi:10.1088/0034-4885/79/9/094504.
 38. Gardner, J. S., Gingras, M. J. P. & Greedan, J. E. Magnetic pyrochlore oxides. *Rev. Mod. Phys.* (2010) doi:10.1103/RevModPhys.82.53.
 39. Rau, J. G. & Gingras, M. J. P. Frustrated quantum rare-earth pyrochlores. *Annual Review of Condensed Matter Physics* (2019) doi:10.1146/annurev-conmatphys-022317-110520.
 40. Snyder, J., Slusky, J. S., Cava, R. J. & Schiffer, P. How ‘spin ice’ freezes. *Nature* (2001) doi:10.1038/35092516.
 41. Gilbert, I., Nisoli, C. & Schiffer, P. Frustration by design. *Phys. Today* (2016) doi:10.1063/PT.3.3237.
 42. Gao, Y. H., Yao, X. P., Li, F. Y. & Chen, G. Spin-1 pyrochlore antiferromagnets: Theory, model, and materials’ survey. *Frontiers of Physics* (2020) doi:10.1007/s11467-020-0974-4.
 43. Matsuhira, K., Wakeshima, M., Hinatsu, Y. & Takagi, S. Metal-insulator transitions in pyrochlore oxides Ln₂Ir₂O₇. *J. Phys. Soc. Japan* (2011) doi:10.1143/JPSJ.80.094701.
 44. Klicpera, M., Vlášková, K. & Diviš, M. Characterization and Magnetic Properties of Heavy Rare-Earth A₂Ir₂O₇Pyrochlore Iridates, the Case of Tm₂Ir₂O₇. *J. Phys. Chem. C* **124**, 20367–20376 (2020).
 45. Nakatsuji, S. *et al.* Metallic spin-liquid behavior of the geometrically frustrated kondo lattice Pr₂Ir₂O₇. *Phys. Rev. Lett.* (2006) doi:10.1103/PhysRevLett.96.087204.
 46. Nakatsuji, S. *et al.* Spontaneous hall effect in the spin liquid phase of Pr₂Ir₂O₇. in *Journal of Physics: Conference Series* vol. 320 012056 (Institute of Physics Publishing, 2011).

-
47. Kondo, T. *et al.* Quadratic Fermi node in a 3D strongly correlated semimetal. *Nat. Commun.* (2015) doi:10.1038/ncomms10042.
 48. Cheng, B. *et al.* Dielectric anomalies and interactions in the three-dimensional quadratic band touching Luttinger semimetal Pr₂Ir₂O₇. *Nat. Commun.* (2017) doi:10.1038/s41467-017-02121-y.
 49. Yang, B. J. & Kim, Y. B. Topological insulators and metal-insulator transition in the pyrochlore iridates. *Phys. Rev. B - Condens. Matter Mater. Phys.* (2010) doi:10.1103/PhysRevB.82.085111.
 50. Savary, L., Moon, E. G. & Balents, L. New type of quantum criticality in the pyrochlore iridates. *Phys. Rev. X* **4**, 041027 (2014).
 51. Yang, Z. & Hao, J. Progress in pulsed laser deposited two-dimensional layered materials for device applications. *Journal of Materials Chemistry C* (2016) doi:10.1039/c6tc01602b.
 52. Akimov, I. A., Sirenko, A. A., Clark, A. M., Hao, J. H. & Xi, X. X. Electric-Field-Induced Soft-Mode Hardening in SrTiO₃ Films. *Phys. Rev. Lett.* **84**, 4625–4628 (2000).
 53. Hao, J., Zhang, Y. & Wei, X. Electric-Induced Enhancement and Modulation of Upconversion Photoluminescence in Epitaxial BaTiO₃:Yb/Er Thin Films. *Angew. Chemie* **123**, 7008–7012 (2011).
 54. B. Roas; L.Schultz. Epitaxial growth of YBa₂Cu₃O_{7-x} thin films by a laser evaporation process. *Appl. Phys. Lett.* **53**, 1557–1559 (1988).
 55. Lee, J. N., Hou, X., Takahashi, R. & Lippmaa, M. Tuning the carrier density in SrTiO₃/LaTiO₃/SrTiO₃ quantum wells. *Appl. Phys. Lett.* **116**, 171601 (2020).
 56. Aziz, M. J. Film growth mechanisms in pulsed laser deposition. *Appl Phys A* **93**, 579–587 (2008).
 57. Venables, J. A., Spiller, G. D. T. & Hanbucken, M. Nucleation and growth of thin films. *Reports on Progress in Physics* (1984) doi:10.1088/0034-4885/47/4/002.
 58. Shin, Y. J. *et al.* Oxygen Partial Pressure during Pulsed Laser Deposition: Deterministic Role on Thermodynamic Stability of Atomic Termination Sequence at SrRuO₃/BaTiO₃ Interface. (2017) doi:10.1021/acsami.7b07813.
 59. Douglas B Chrisey, G. K. H. *Pulsed Laser Deposition of Thin Films. Pulsed Laser Deposition of Thin Films* (John Wiley & Sons, Inc., 2006). doi:10.1002/0470052120.
 60. Ohnishi, T., Lippmaa, M., Yamamoto, T., Meguro, S. & Koinuma, H. Improved stoichiometry and misfit control in perovskite thin film formation at a critical fluence by pulsed laser deposition. *Appl. Phys. Lett.* **87**, 1–3 (2005).

-
61. Zhaoyang, W., Liyuan, S. & Lizhong, H. Effect of laser repetition frequency on the structural and optical properties of ZnO thin films by PLD. *Vacuum* **85**, 397–399 (2010).
 62. Johnson, B. C., McCallum, J. C. & Aziz, M. J. Solid-Phase Epitaxy. in *Handbook of Crystal Growth: Thin Films and Epitaxy: Second Edition* vol. 3 317–363 (Elsevier Inc., 2015).
 63. Fujita, T. C. *et al.* Odd-parity magnetoresistance in pyrochlore iridate thin films with broken time-reversal symmetry. *Sci. Rep.* **5**, (2015).
 64. Ohtsuki, T., Tian, Z., Halim, M., Nakatsuji, S. & Lippmaa, M. Growth of Pr₂Ir₂O₇ thin films using solid phase epitaxy. *J. Appl. Phys.* **127**, 35303 (2020).
 65. Ohtsuki, T. *et al.* Strain-induced spontaneous Hall effect in an epitaxial thin film of a Luttinger semimetal. *Proc. Natl. Acad. Sci. U. S. A.* **116**, 8803–8808 (2019).
 66. Jin Kim, W. *et al.* Strain engineering of the magnetic multipole moments and anomalous Hall effect in pyrochlore iridate thin films. <http://advances.sciencemag.org/> (2020).
 67. Guo, L. *et al.* Spontaneous Hall effect enhanced by local Ir moments in epitaxial Pr₂Ir₂O₇ thin films. *Phys. Rev. B* **101**, 104405 (2020).
 68. Gallagher, J. C. *et al.* Epitaxial growth of iridate pyrochlore Nd₂Ir₂O₇ films. *Sci. Rep.* **6**, 1–7 (2016).
 69. Sellappan, P., Tang, C., Shi, J. & Garay, J. E. An integrated approach to doped thin films with strain-tunable magnetic anisotropy: powder synthesis, target preparation and pulsed laser deposition of Bi:YIG. *Mater. Res. Lett.* (2017) doi:10.1080/21663831.2016.1195779.
 70. Saheb, N. *et al.* Spark plasma sintering of metals and metal matrix nanocomposites: A review. *Journal of Nanomaterials* vol. 2012 (2012).
 71. Binnig, G., Quate, C. F. & Gerber, C. Atomic force microscope. *Phys. Rev. Lett.* **56**, 930–933 (1986).
 72. Garcia, R. Nanomechanical mapping of soft materials with the atomic force microscope: methods, theory and applications. *This J. is Cite this Chem. Soc. Rev* **5850**, 5850 (2020).
 73. Aguilar-Marín, P., Angelats-Silva, L., Noriega-Diaz, E., Chavez-Bacilio, M. & Verde-Vera, R. Understanding the phenomenon of x-ray diffraction by crystals and related concepts. *Eur. J. Phys.* (2020) doi:10.1088/1361-6404/ab8e53.
 74. Millican, J. N. *et al.* Crystal growth and structure of R₂Ir₂O₇ (R = Pr, Eu) using molten KF. *Mater. Res. Bull.* (2007) doi:10.1016/j.materresbull.2006.08.011.

-
75. Wang, Z., Zhou, G., Jiang, D. & Wang, S. Recent development of A₂B₂O₇ system transparent ceramics. *Journal of Advanced Ceramics* (2018) doi:10.1007/s40145-018-0287-z.
 76. Turner, K. M. *et al.* Pressure-induced structural modifications of rare-earth hafnate pyrochlore. *J. Phys. Condens. Matter* (2017) doi:10.1088/1361-648X/aa7148.
 77. Lippmaa, M., Kawasaki, S., Takahashi, R. & Yamamoto, T. Noble metal clustering and nanopillar formation in an oxide matrix. *Japanese Journal of Applied Physics* (2020) doi:10.7567/1347-4065/ab57e2.
 78. Gazulla, M. F. *et al.* Praseodymium oxides. Complete characterization by determining oxygen content. *Microchem. J.* **148**, 291–298 (2019).
 79. Yang, W. C. *et al.* Stoichiometry control and electronic and transport properties of pyrochlore B₂Ir₂O₇ thin films. *Phys. Rev. Mater.* (2018) doi:10.1103/PhysRevMaterials.2.114206.
 80. Schütz, P. *et al.* Electronic structure of epitaxial perovskite films in the two-dimensional limit: Role of the surface termination. *Appl. Phys. Lett.* (2020) doi:10.1063/5.0002985.
 81. Scharf, T. & Krebs, H. U. Influence of inert gas pressure on deposition rate during pulsed laser deposition. *Appl. Phys. A Mater. Sci. Process.* (2002) doi:10.1007/s00339-002-1442-4.
 82. Nishimine, H., Wakeshima, M. & Hinatsu, Y. Crystal structures, magnetic and thermal properties of Ln₃IrO₇ (Ln=Pr, Nd, Sm, and Eu). *J. Solid State Chem.* (2004) doi:10.1016/j.jssc.2003.08.036.
 83. Guo, L. *et al.* Route to in situ synthesis of epitaxial Pr₂Ir₂O₇ thin films guided by thermodynamic calculations. *arXiv* (2020).
 84. Yang, J. *et al.* Frustration-induced non-Curie-Weiss paramagnetism in La₃Ir₃O₁₁: A fractional valence state iridate. *Phys. Rev. B* (2019) doi:10.1103/PhysRevB.100.205107.
 85. Patra, A., Jana, S., Constantin, L. A., Chiodo, L. & Samal, P. Improved transition metal surface energies from a generalized gradient approximation developed for quasi two-dimensional systems. *J. Chem. Phys.* (2020) doi:10.1063/1.5145367.
 86. Asadian, M. The Influence of Atmosphere on Oxides Crystal Growth. in *Modern Aspects of Bulk Crystal and Thin Film Preparation* (2012). doi:10.5772/29648.
 87. Seo, I., Yokota, S., Imai, Y. & Gohda, Y. First-principles calculations on high-temperature desorption loss from iridium. *Comput. Mater. Sci.* (2020) doi:10.1016/j.commatsci.2020.109897.